JM PAPERS

Self-similar mechanisms in wall turbulence studied using resolvent analysis

U. Karban[1,2,†], E. Martini[1], A.V.G. Cavalieri[3], L. Lesshafft[4] and P. Jordan[1]

[1]Département Fluides, Thermique, Combustion, Institut Pprime, CNRS-University of Poitiers-ENSMA, France

[2]Department of Aerospace Engineering, Middle East Technical University, Ankara 06800, Turkey

[3]Instituto Tecnológico de Aeronáutica, São José dos Campos/SP, Brazil

[4]Laboratoire d'Hydrodynamique, CNRS / École polytechnique, Institut Polytechnique de Paris, Palaiseau, France

Self-similarity of wall-attached coherent structures in a turbulent channel at $Re_\tau = 543$ is explored by means of resolvent analysis. In this modelling framework, coherent structures are understood to arise as a response of the linearised mean-flow operator to generalised frequency-dependent Reynolds stresses, considered to act as an endogenous forcing. We assess the self-similarity of both the wall-attached flow structures and the associated forcing. The former are educed from direct numerical simulation data by finding the flow field correlated with the wall shear, whereas the latter is identified using a frequency space version of extended proper orthogonal decomposition (Borée, *Exp. Fluids*, vol. 35, issue 2, 2003, pp. 188–192). The forcing structures identified are compared to those obtained using the resolvent-based estimation introduced by Towne et al. (*J. Fluid Mech.*, vol. 883, 2020, A17). The analysis reveals self-similarity of both wall-attached structures – in quantitative agreement with Townsend's hypothesis of self-similar attached eddies – and the underlying forcing, at least in certain components.

1. Introduction

The study of coherent structures in turbulent flow dates back to the early 1950s. Since the first observations of these organised motions, for instance by Townsend (1951, 1976), Mollo-Christensen (1967) and Crow & Champagne (1971), a substantial body of work has been dedicated to developing an understanding of how they work and what dynamical

† Email address for correspondence: ukarban@metu.edu.tr

role they play. Reviews for wall-bounded flow have been provided by Robinson (1991) and Jiménez (2012).

Coherent structures can be seen in flow visualisations or simulations of boundary layers, where they are manifest in the form of streaks (Wu & Moin 2009; Eitel-Amor *et al.* 2015; Jodai & Elsinga 2016) or hairpin-like structures (Adrian 2007). They may be analysed quantitatively in terms of their statistics and compared with frequency space models (Sen, Bhaganagar & Juttijudata 2007; Baltzer, Adrian & Wu 2010; Jordan & Colonius 2013; Cavalieri, Jordan & Lesshafft 2019; Lesshafft *et al.* 2019; Abreu *et al.* 2020*b*; Morra *et al.* 2021; Nogueira *et al.* 2021). A recent overview of the different structures observed in wall-bounded turbulent flows, the focus of this study, can be found in Lee & Jiang (2019).

An early modelling idea, where wall-bounded flows are concerned, is that of the attached-eddy hypothesis (AEH), introduced by Townsend (1951, 1976) and further developed by Perry & Chong (1982). Underlying this hypothesis is the idea that eddies in the logarithmic region of wall-bounded turbulent flows extend to the wall. This implies that their characteristic dimensions scale with distance to the wall, which implies, in turn, the existence of a self-similar organisation. A recent review of the literature on the AEH can be found in Marusic & Monty (2019).

The original AEH considers coherent structures in the logarithmic region of boundary layers (Townsend 1976) at high Reynolds number (Re), and predicts an α^{-1} decay in the one-dimensional energy spectrum, where α is the streamwise wavenumber. The α^{-1} decay was observed in wall-bounded turbulent flows at friction Reynolds number $Re_\tau \sim 100\,000$ (Perry, Henbest & Chong 1986; Chandran *et al.* 2017), suggesting the existence of attached eddies that dominate the kinetic energy in the logarithmic region. The high Reynolds number of those studies makes it difficult to conclude on the validity of the AEH in flows simulated numerically or studied at laboratory scale with low or moderate Reynolds number. Cheng *et al.* (2020) showed that wall-attached structures account for a significant portion of the flow energy even at low-Re flows, ranging from $Re_\tau = 180$ to 1000. They extracted the structures that move together and reach up to the wall, and observed geometric self-similarity among these structures. Chandran, Monty & Marusic (2020) investigated the two-dimensional spectra of the streamwise velocity component, where a transition from $\alpha^{-1/2}$ to α^{-1} scaling was observed as moving from $Re_\tau = 2400$ to $26\,000$. Davidson, Krogstad & Nickels (2006*a*) and Davidson, Nickels & Krogstad (2006*b*) showed that the α^{-1} decay is not observed at lower Reynolds numbers, and they attributed this to the limited range of scales of attached eddy that can exist at low Re, whence their smaller contribution to the energy spectrum. In view of this, they suggested using the second-order structure function as a better indicator of attached eddies. Agostini & Leschziner (2017) used structure functions to show that attached-eddy behaviour can be observed at wall-normal distance, y^+, ranging from 80 to 2000 in channel flow at $Re_\tau = 4200$. Their study demonstrated that choosing the correct method to identify attached eddies, as statistical entities, is crucial in finding evidence of the AEH in turbulent flows that are attainable at lab scale or via numerical simulation.

There exist many techniques for the detection of coherent structures. One may use two-point measurements (Tomkins & Adrian 2003; Monty *et al.* 2007; Baars, Hutchins & Marusic 2017), conditional sampling (Hussain 1986; Hwang *et al.* 2016; Cheng *et al.* 2020; Hwang, Lee & Sung 2020) or modal decomposition techniques such as proper orthogonal decomposition (POD) (Lumley 1967), dynamic mode decomposition (DMD) (Schmid 2010) or spectral proper orthogonal decomposition (SPOD) (Lumley 1970; Picard & Delville 2000; Schmidt *et al.* 2018; Towne, Schmidt & Colonius 2018). A review of these decomposition techniques, except SPOD, can be found in Taira *et al.* (2017). It has been

demonstrated how POD can be used to educe attached eddies in pipe flows at $Re_\tau = 1300$ (Hellström, Marusic & Smits 2016) and at $Re_\tau = 685$ (Hellström & Smits 2017). Those studies showed how leading POD modes are self-similar and scale with distance to the wall. This is in line with Townsend's original hypothesis, which states that attached eddies correspond to the most energetic motions of the boundary layer (Townsend 1976).

Coherent structures obtained through the aforementioned decomposition techniques do not satisfy the Navier–Stokes equations. An attached-eddy model based, for instance, on similarity analyses such as discussed above, provides a kinematic description only. A number of studies have shown, using dynamical descriptions, how the energy-containing motions at different scales in turbulent wall-bounded flows may be maintained through a self-sustaining mechanism (see Cossu & Hwang (2017) for a review on the subject). Those studies rely on overdamped large-eddy simulations of the filtered Navier–Stokes equations (Hwang & Cossu 2010*b*; Hwang 2015), and they show that the self-sustaining cycle exhibits self-similarity. We here use standard direct numerical simulations (DNS) coupled with the resolvent framework to investigate such self-similar dynamics for the wall-attached structures in the flow.

Resolvent analysis provides a dynamical framework to study coherent structures and the nonlinear interactions that drive them (Hwang & Cossu 2010*a*; McKeon & Sharma 2010; Schmidt *et al.* 2018; Cavalieri *et al.* 2019; Lesshafft *et al.* 2019). The approach involves linearising the Navier–Stokes equations about the mean flow and retaining the nonlinear terms as an inhomogeneous forcing of the linearised system. The problem can then be cast in an input/output (forcing/response) form, with forcing and response connected by the resolvent operator. Optimal forcing–response mode pairs can be identified from the resolvent operator, revealing the most important linear growth mechanisms in the flow. In many flows, the leading response mode is found to match closely coherent structures educed from time-resolved flow data (McKeon & Sharma 2010; Lesshafft *et al.* 2019). It has been shown in the literature (Hwang & Cossu 2010*a*; Moarref *et al.* 2013; McKeon 2017; Sharma, Moarref & McKeon 2017, among others) that for wall-bounded flows, the optimal response mode exhibits a self-similar structure reminiscent of attached eddies. However, the dynamics of coherent structures are ultimately determined by the details of the nonlinear interactions at work in the flow, and these must be considered in order to understand how forcing/response modes of the resolvent operator combine to produce the observed behaviour (Zare, Jovanović & Georgiou 2017; Rosenberg, Symon & McKeon 2019; Pickering *et al.* 2019; Martini *et al.* 2020; Morra *et al.* 2021; Nogueira *et al.* 2021; Symon, Illingworth & Marusic 2021). Consideration of the resolvent operator alone can provide only a limited understanding of the dynamics of attached eddies in wall-bounded flows. It is this that motivates the study that we undertake, where a data-driven approach is elaborated to explore the self-similarity of wall-attached coherent structures *and* the nonlinear interactions that drive them. It is important to understand if the self-similarity seen in the flow structures is imposed only by the resolvent operator or if a self-similar forcing also plays a role. The former scenario implies that nonlinear terms, although not self-similar, are filtered by the self-similar resolvent operator such that the response is self-similar. The latter scenario, on the other hand, indicates a dynamic self-similarity, which can be useful for modelling wall-shear-related phenomena in turbulent flows.

Our objective is to identify forcing structures that exist in the data and are associated with observed wall-attached coherent structures. One approach that can be used to do this has been proposed by Towne, Lozano-Durán & Yang (2020), where a resolvent-based estimation (RBE) of forcing statistics was achieved by combining flow measurements with the resolvent operator. Martini *et al.* (2020) extended that work by proposing an optimal

estimation approach by which the space–time forcing field can be computed from a limited set of flow measurements; the estimator requires a model for the forcing statistics. RBE is recovered when a white model forcing is assumed, showing that this is an underlying assumption of the RBE method.

In this work, we adopt an alternative approach, in which the extended proper orthogonal decomposition (EPOD) of Borée (2003), which we cast in frequency space, is applied in the resolvent framework so as to identify forcing structures that are associated with an observed coherent structure. This method was first discussed in Towne *et al.* (2015). We refer to this tailored implementation of EPOD as resolvent-based extended spectral proper orthogonal decomposition (RESPOD). Related methods are observable inferred decomposition (OID) (Schlegel *et al.* 2012) and approaches based on linear stochastic estimation, such as in Kerherve *et al.* (2012). In each of these cases, linear mappings are identified between a selected observable and some other field considered to drive that observable (the flow structures in a jet responsible for sound radiation, for example). But linear mappings so identified are not grounded in any rigorous dynamic framework. The advantage of the RESPOD method is that a dynamic relation is granted within the resolvent framework. Empirically observed coherent structures are used to identify the forcing structures that exist in unsteady data and that drive the coherent structures via the resolvent operator. The dynamic relationship between forcing and response is identified such that it is consistent with the linearised Navier–Stokes equations. We use this approach to find coherent structures that are correlated to the wall shear, i.e. that are wall-attached, and the associated forcing.

A related effort is the work of Skouloudis & Hwang (2021), who superpose resolvent modes with various wavenumbers, as a representation of attached eddies, so as to recover the Reynolds shear stress of channels. This is referred to as a quasi-linear approximation (QLA), which may be seen as a dynamic model of attached eddies based on the linearised Navier–Stokes operator. For simplicity, the superposition is restricted to zero streamwise wavenumber, and, for most cases, to zero frequency. As discussed in the cited paper, even with restricted wavenumbers and frequencies, such a superposition is non-unique, as there are several combinations of forcing modes that lead to the same overall Reynolds shear stress. While the approach of Skouloudis & Hwang (2021) leads to correct Reynolds number trends, a quantitative comparison with simulation data reveals differences. Information on nonlinear terms driving flow responses may be built into dynamic attached-eddy models for more accurate predictions. We anticipate that self-similarity may be identified in both forcing and response modes with the techniques that we aim to use in the present study. Use of the educed self-similar forcing in QLA is expected to lead to structures that better match fluctuations in wall-bounded turbulence.

As we will discuss (§ 2), RESPOD is related to the RBE method of Towne *et al.* (2020). RBE provides the 'observable' forcing that has the minimal norm required to generate the observed coherent structure, and it eliminates all 'silent' components of forcing, i.e. those components that, while present in the data, do not drive the response directly. We will show that RESPOD finds, for a given coherent structure, all the correlated forcing, including the silent components. These silent components, though redundant in terms of the direct driving of coherent structures through the resolvent operator, provide additional information regarding the forcing mechanisms at play, and, considered together with the 'non-silent', driving components, provide a more complete picture of the forcing structures that actually exist in the unsteady data and are correlated with the observed coherent structures. We thus obtain a more complete description of attached eddies and the scale interactions by which they are driven.

This paper is organised as follows. In § 2, the RBE and RESPOD methods are revisited. The characteristics of the two methods are discussed via implementation on a toy model. The methods are then applied in a turbulent channel flow problem in § 3. A DNS database with friction Reynolds number $Re_\tau = 543$ is used. The methodology to trace attached eddies in the turbulent channels and to compute the associated forcing is presented with the results. Further discussions are provided in § 4.

2. Identifying the forcing associated with optimal response

2.1. *Resolvent-based estimation*

We consider the Navier–Stokes equations

$$\boldsymbol{M}\,\partial_t \boldsymbol{q}(\boldsymbol{x}, t) = \mathcal{N}(\boldsymbol{q}(\boldsymbol{x}, t)), \tag{2.1}$$

where $\boldsymbol{q} = [\rho,\, u,\, v,\, w,\, p]^{\mathrm{T}}$ is the state vector, $\mathcal{N}$ denotes the nonlinear Navier–Stokes operator, and the matrix $\boldsymbol{M}$ is zero for the continuity equation and identity matrix for the rest in incompressible flows, or the identity matrix in compressible flows. Discretisation in space and linearisation around the mean, $\bar{\boldsymbol{q}}(\boldsymbol{x})$, yields

$$\boldsymbol{M}\,\partial_t \boldsymbol{q}'(\boldsymbol{x}, t) - \boldsymbol{A}(\boldsymbol{x})\,\boldsymbol{q}'(\boldsymbol{x}, t) = \boldsymbol{f}(\boldsymbol{x}, t), \tag{2.2}$$

where $\boldsymbol{A}(\boldsymbol{x}) = \partial_q \mathcal{N}|_{\bar{q}}$ is the linear operator obtained from the Jacobian of $\mathcal{N}$, and $\boldsymbol{f}(\boldsymbol{x}, t)$ denotes all the remaining nonlinear terms, interpreted as a forcing term in the above equation. The equations are linearised using primitive variables (Karban *et al.* 2020). In the resolvent framework, (2.2) is Fourier transformed and rearranged to obtain

$$\hat{\boldsymbol{q}}(\boldsymbol{x}, \omega) = \boldsymbol{R}(\boldsymbol{x}, \omega)\,\hat{\boldsymbol{f}}(\boldsymbol{x}, \omega), \tag{2.3}$$

where $\boldsymbol{x} = [x,\, y,\, z]^{\mathrm{T}}$ is the space vector, ω is the angular frequency, the hat indicates a Fourier transformed quantity, and $\boldsymbol{R}(\boldsymbol{x}, \omega) = (-\mathrm{i}\omega\boldsymbol{M} - \boldsymbol{A}(\boldsymbol{x}))^{-1}$ is the resolvent operator. In what follows, notation showing dependence on $\boldsymbol{x}$ and ω will be dropped for brevity.

The cross-spectral densities of the response and forcing can also be related via the resolvent operator

$$\boldsymbol{S} = \boldsymbol{R}\boldsymbol{P}\boldsymbol{R}^H, \tag{2.4}$$

where $\boldsymbol{S} = \mathrm{E}\{\hat{\boldsymbol{q}}\hat{\boldsymbol{q}}^H\}$ and $\boldsymbol{P} = \mathrm{E}\{\hat{\boldsymbol{f}}\hat{\boldsymbol{f}}^H\}$ denote the response and forcing cross-spectral density (CSD) matrices, respectively, with $\mathrm{E}\{\cdot\}$ denoting the expectation operator obtained by averaging different realisations, and the superscript H denoting the conjugate transpose, or Hermitian.

The resolvent operator can be modified in order to explore the relationship between subsets of the forcing and response. For instance, limited measurements at a selection of points, $\hat{\boldsymbol{y}}$, may be considered and related to forcing:

$$\hat{\boldsymbol{y}} = \boldsymbol{C}\hat{\boldsymbol{q}}, \tag{2.5}$$

$$\hat{\boldsymbol{y}} = \tilde{\boldsymbol{R}}\hat{\boldsymbol{f}}, \tag{2.6}$$

where $\boldsymbol{C}$ denotes the measurement matrix and $\tilde{\boldsymbol{R}} \triangleq \boldsymbol{C}\boldsymbol{R}$ is the modified resolvent operator that connects forcing to those measurements. We will first investigate the case where $\boldsymbol{C} = \boldsymbol{I}$ and $\boldsymbol{R}$ is full-rank, i.e. $\tilde{\boldsymbol{R}}$ is also full-rank, before extending our analysis to cases where $\tilde{\boldsymbol{R}}$ may be singular. Note that (2.2) and (2.3) are exact and provide a bijective relation between

the forcing and the response when the resolvent operator is full-rank, and an injective relation when $\boldsymbol{R}$ is singular.

We employ SPOD to identify coherent structures in the flow. This requires definition of an inner product

$$\langle \boldsymbol{a}, \boldsymbol{b} \rangle = \int_{\Omega} \boldsymbol{b}^H \mathcal{W} \boldsymbol{a} \, \mathrm{d}\boldsymbol{x}, \tag{2.7}$$

where $\mathcal{W}$ denotes an energy norm. Equation (2.7) can be written in discrete form as

$$\langle \boldsymbol{a}, \boldsymbol{b} \rangle = \boldsymbol{b}^H \boldsymbol{W} \boldsymbol{a}, \tag{2.8}$$

where $\boldsymbol{W}$ now accounts for both the energy norm and the numerical quadrature weights. The SPOD modes, which are orthogonal with respect to the inner product defined by (2.8), are obtained by solving the eigenvalue problem

$$\boldsymbol{S} \boldsymbol{W} \boldsymbol{\psi} = \lambda \boldsymbol{\psi}, \tag{2.9}$$

where $\boldsymbol{\psi}$ and λ denote the eigenvector (SPOD mode) and the eigenvalue (SPOD mode mean square value). The CSD matrix $\boldsymbol{S}$ can be built from SPOD modes as

$$\boldsymbol{S} = \sum_n \lambda_n \boldsymbol{\psi}_n \boldsymbol{\psi}_n^H, \tag{2.10}$$

where the subscript n denotes SPOD mode number.

For non-singular $\boldsymbol{R}$, the forcing mode that generates a given SPOD mode, $\boldsymbol{\psi}$, can be obtained by inverting the resolvent equation

$$\boldsymbol{\phi} = \boldsymbol{L} \boldsymbol{\psi}, \tag{2.11}$$

where $\boldsymbol{L} \triangleq (-\mathrm{i}\omega\boldsymbol{M} - \boldsymbol{A})$ and $\boldsymbol{R} = \boldsymbol{L}^{-1}$. In the case of $\tilde{\boldsymbol{R}}$, which is singular, direct inversion is not possible, and the forcing mode associated with the SPOD mode, $\boldsymbol{\psi}$, can then be obtained by means of a pseudo-inverse of $\tilde{\boldsymbol{R}}$:

$$\boldsymbol{\phi} = \tilde{\boldsymbol{R}}^+ \boldsymbol{\psi}. \tag{2.12}$$

The mode $\boldsymbol{\phi}$ in (2.12) can be understood as the minimal-norm forcing that creates the response, $\boldsymbol{\psi}$, through the resolvent operator, in what is called resolvent-based estimation (RBE) (Martini *et al.* 2020; Towne *et al.* 2020). The forcing structures that are correlated with the response but are 'silent', i.e. have no flow response, are not present in the forcing modes estimated using RBE. This might be a desired property for the kinematic modelling of forcing, as whatever is included in the estimated mode is ensured to contribute to the response. However, from a dynamical modelling point of view, elimination of the correlated-but-silent parts of the forcing may hide important dynamic traits of the interaction mechanisms that underpin the forcing structures. Since the silent components are correlated to the observable forces, they are likely generated by the same mechanisms. Thus their study can facilitate identification of these mechanisms. To identify such structures, we consider, in what follows, a data-driven approach that takes into account the forcing and response structures that are actually contained in the data.

2.2. *Resolvent-based extended spectral proper orthogonal decomposition*

The approach that we present is adapted from the EPOD of Borée (2003), whose goal was to identify correlations between an observed POD mode and some other target field.

In Hoarau *et al.* (2006), the method was used in spectral domain. We revisit EPOD also in frequency space, setting the target event as the forcing defined by (2.3). This specific construction of EPOD was first discussed in Towne *et al.* (2015). We refer here to this implementation as 'resolvent-based, extended spectral proper orthogonal decomposition' (RESPOD).

The SPOD modes defined by (2.9) are orthogonal with respect to the norm defined by (2.8), i.e.

$$\langle \boldsymbol{\psi}_n, \boldsymbol{\psi}_p \rangle = \delta_{np}, \tag{2.13}$$

where $\boldsymbol{\psi}_n$ is the nth SPOD mode. The SPOD modes provide a complete basis that can be used to expand any realisation of the state vector as

$$\hat{q} = \sum_n a_n \boldsymbol{\psi}_n, \tag{2.14}$$

where the projection coefficient a_n associated with the nth eigenmode is obtained by the projection

$$a_n = \langle \hat{q}, \boldsymbol{\psi}_n \rangle. \tag{2.15}$$

The orthonormality of the SPOD basis, defined by (2.13), imposes that the projection coefficients satisfy

$$\mathrm{E}\{a_n a_p^H\} = \lambda_n \delta_{np}. \tag{2.16}$$

This can be seen as follows:

$$
\begin{aligned}
\mathrm{E}\{a_n a_p^H\} &= \mathrm{E}\{\langle \hat{q}, \boldsymbol{\psi}_n \rangle \langle \hat{q}, \boldsymbol{\psi}_n \rangle^H\} \\
&= \mathrm{E}\{\boldsymbol{\psi}_n^H \boldsymbol{W} \hat{q} \hat{q}^H \boldsymbol{W}^H \boldsymbol{\psi}_p\} \quad \text{(using (2.8))} \\
&= \boldsymbol{\psi}_n^H \boldsymbol{W} \mathrm{E}\{\hat{q} \hat{q}^H\} \boldsymbol{W}^H \boldsymbol{\psi}_p \\
&= \boldsymbol{\psi}_n^H \boldsymbol{W} \sum_k \lambda_k \boldsymbol{\psi}_k \boldsymbol{\psi}_k^H \boldsymbol{W}^H \boldsymbol{\psi}_p \quad \text{(using (2.10))} \\
&= \lambda_n \delta_{np}.
\end{aligned}
\tag{2.17}
$$

Here, the expectation operator corresponds to an ensemble average of Fourier realisations. Borée (2003) used (2.14) and (2.16) to show that

$$
\begin{aligned}
\mathrm{E}\{\hat{q} \, a_p^H\} &= \mathrm{E}\left\{\left(\sum_n a_n \boldsymbol{\psi}_n\right) a_p^H\right\} \\
&= \sum_n \mathrm{E}\{a_n a_p^H\} \boldsymbol{\psi}_n \\
&= \lambda_p \boldsymbol{\psi}_p,
\end{aligned}
\tag{2.18}
$$

which provides an alternative way to compute $\boldsymbol{\psi}_p$ as

$$\boldsymbol{\psi}_p = \frac{\mathrm{E}\{\hat{q} \, a_p^H\}}{\lambda_p}, \tag{2.19}$$

assuming that a_p is known. Equation (2.19) corresponds to the snapshot approach, shown by Towne *et al.* (2018) to provide a less costly alternative to eigendecomposition of (2.9).

Note that for this, one needs to calculate the projection coefficients beforehand. Using the decomposition given in (2.14), we can show that

$$\langle \hat{q}, \hat{q} \rangle = \sum_n a_n a_n^H. \tag{2.20}$$

For a given $\hat{Q}$ defined as the set of realisations of $\hat{q}$, (2.20) can be written as

$$\langle \hat{Q}, \hat{Q} \rangle = \sum_n a_n a_n^H, \tag{2.21}$$

where $a_n \triangleq \langle \hat{Q}, \psi_n \rangle$ denotes the projection coefficient vector. Note that (2.16) holds also for a_n, implying the orthogonality of the projection coefficient vectors that correspond to different SPOD modes. Given this orthogonality, rewriting (2.21) by normalising a_n with $\lambda_n^{-1/2}$ as

$$\langle \hat{Q}, \hat{Q} \rangle = \sum_n (a_n \lambda_n^{-1/2}) \lambda_n (a_n^H \lambda_n^{-1/2}), \tag{2.22}$$

we obtain the eigendecomposition of $\langle \hat{Q}, \hat{Q} \rangle$. Computing the eigendecomposition given in (2.22), one can obtain the projection coefficients before calculating the SPOD vectors.

Given the forcing vector $\hat{f}$, its RESPOD mode is given by

$$\chi_p = \frac{\mathrm{E}\{\hat{f} a_p^H\}}{\lambda_p}. \tag{2.23}$$

The RESPOD mode χ_p provides the forcing mode associated with the pth SPOD mode of the response. In Borée (2003), it was shown that the extended modes can be used to isolate, from the target event, the part that is correlated with the observed coherent structure. Given, for instance, the rank-1 representation of $\hat{q}$ as $\hat{q}_1 = a_1 \psi_1$, the corresponding RESPOD mode χ_1 allows identification of $\hat{f}_1 \triangleq a_1 \chi_1$, which is the forcing correlated with $\hat{q}_1$. This can be seen by comparing the two cross-covariances between the forcing and the response given as

$$\begin{aligned} \mathrm{E}\{\hat{f} \hat{q}_1^H\} &= \mathrm{E}\{\hat{f} a_1^H \psi_1^H\} \\ &= \mathrm{E}\{\hat{f} a_1^H\} \psi_1^H \\ &= \lambda_1 \chi_1 \psi_1^H \end{aligned} \tag{2.24}$$

and

$$\begin{aligned} \mathrm{E}\{\hat{f}_1 \hat{q}_1^H\} &= \mathrm{E}\{a_1 \chi_1 a_1^H \psi_1^H\} \\ &= \chi_1 \mathrm{E}\{a_1 a_1^H\} \psi_1^H \\ &= \lambda_1 \chi_1 \psi_1^H. \end{aligned} \tag{2.25}$$

This indicates that $\hat{f}_1$ contains all the forcing that is correlated with $\hat{q}_1$.

939 A36-8

As the target event we consider here is the forcing term in the resolvent framework, which satisfies (2.6), substituting (2.6) into (2.19), we can show that

$$\boldsymbol{\psi}_p = \frac{\mathrm{E}\{\tilde{\boldsymbol{R}}\hat{f}a_p^H\}}{\lambda_p}$$

$$= \tilde{\boldsymbol{R}}\frac{\mathrm{E}\{\hat{f}a_p^H\}}{\lambda_p}$$

$$= \tilde{\boldsymbol{R}}\boldsymbol{\chi}_p, \qquad (2.26)$$

indicating that the correlated response and force modes are dynamically consistent, i.e. they satisfy (2.6).

As mentioned earlier, the relation between forcing and response becomes bijective for a non-singular resolvent operator; i.e. for a given response $\boldsymbol{\psi}$, there is a unique forcing mode that satisfies (2.26) and (2.11). This implies that for the non-singular resolvent operator, the forcing mode identified by RESPOD becomes identical to the RBE mode predicted using (2.11). But for the case of a singular resolvent operator, RESPOD finds both the minimal-norm forcing (also predicted by RBE) necessary to generate the SPOD mode *and* the correlated-but-silent components of the nonlinear scale interactions.

2.3. *Comparison of RBE and RESPOD using a simple model*

As a toy model to illustrate the techniques, we consider two rank-3 resolvent operators, $\boldsymbol{R}_f$ and $\boldsymbol{R}_s$, that are, respectively, full-rank and singular:

$$\boldsymbol{R}_f = \begin{bmatrix} 3 & 0 & 0 \\ 0 & 2 & 0 \\ 0 & 0 & 1 \end{bmatrix}, \quad \boldsymbol{R}_s = \begin{bmatrix} 3 & 0 & 0 & 0 & 0 \\ 0 & 2 & 0 & 0 & 0 \\ 0 & 0 & 1 & 0 & 0 \end{bmatrix}. \qquad (2.27a,b)$$

Both systems are driven by random forcing vectors, $\hat{\boldsymbol{f}}_f = [c_1, c_2, c_3]^{\mathrm{T}}$ and $\hat{\boldsymbol{f}}_s = [c_1, c_2, c_3, 3c_1, c_4]^{\mathrm{T}}$, respectively, where c_i is a random number with zero mean and unit variance. The random forcing realisations are generated using Matlab random number generator. The random number seeding is re-initialised for each simulation to ensure using the same random value series, which makes the results repeatable. The fourth and fifth components in $\hat{\boldsymbol{f}}_s$ project onto the null space of $\boldsymbol{R}_s$, but the fourth component is fully correlated to the first since both contain the same random variable, c_1. Re-initialisation of the random number generator ensures that the first three components of $\hat{\boldsymbol{f}}_f$ and $\hat{\boldsymbol{f}}_s$, those that are observable through the corresponding resolvent operators, are identical. The responses obtained for the two systems are thereby identical. Two tests are carried out using 10 and 500 realisations, respectively. The leading SPOD mode for both singular and non-singular systems is obtained as $\boldsymbol{\psi} = [-0.9622, 0.2576, -0.0890]^{\mathrm{T}}$ when 10 realisations are considered, and $\tilde{\boldsymbol{\psi}} = [-0.9943, -0.1056, 0.0148]^{\mathrm{T}}$ with 500 realisations. As the forcing in the full-rank model problem is white, i.e. $\boldsymbol{P} = \boldsymbol{I}$, by inspection, one can see that the expected value for the leading SPOD mode is $\boldsymbol{\psi} = [1, 0, 0]^{\mathrm{T}}$ (or its negative). The predictions based on realisations converge to the expected value with an algebraic convergence.

Using 10 realisations, the forcing modes computed using RBE and RESPOD, respectively $\phi_{f/s}$ and $\chi_{f/s}$, are, for the full-rank system,

$$\phi_f = \begin{bmatrix} -0.3207 \\ 0.1288 \\ -0.0890 \end{bmatrix} \quad \text{and} \quad \chi_f = \begin{bmatrix} -0.3207 \\ 0.1288 \\ -0.0890 \end{bmatrix}, \qquad (2.28a,b)$$

while for the singular system we obtain

$$\phi_s = \begin{bmatrix} -0.3207 \\ 0.1288 \\ -0.0890 \\ 0 \\ 0 \end{bmatrix} \quad \text{and} \quad \chi_s = \begin{bmatrix} -0.3207 \\ 0.1288 \\ -0.0890 \\ -0.9622 \\ 0.0283 \end{bmatrix}. \qquad (2.29a,b)$$

The same results for the cases based on 500 realisations are given as

$$\phi_f = \begin{bmatrix} -0.3314 \\ -0.0528 \\ 0.0148 \end{bmatrix}, \quad \chi_f = \begin{bmatrix} -0.3314 \\ -0.0528 \\ 0.0148 \end{bmatrix}, \quad \phi_s = \begin{bmatrix} -0.3314 \\ -0.0528 \\ 0.0148 \\ 0 \\ 0 \end{bmatrix} \quad \text{and} \quad \chi_s = \begin{bmatrix} -0.3314 \\ -0.0528 \\ 0.0148 \\ -0.9943 \\ 0.0066 \end{bmatrix}.$$

$$(2.30a\text{--}d)$$

As expected, the results obtained using RBE and RESPOD are identical in the full-rank system. The fourth component of χ_s is three times the first component, where this correlation information was included in the definition of $\hat{f}_s$. Although the RBE method, which finds the minimal-norm forcing for a given response, and the RESPOD method, which finds the correlated forcing for a given response, ask different questions, their results are the same when the resolvent operator is full-rank. This is because for a full-rank resolvent operator, no silent forcing exists. When different numbers of realisations are considered, RBE and RESPOD yield identical results when the resolvent operator is full-rank; this is because the SPOD response mode and the RESPOD forcing mode have identical convergence in that case. This will be the case when the two methods are based on the exact same realisations, and the realisations are consistent, i.e. they satisfy (2.6). The results may differ if the database contains noise on the response and/or the forcing, which is outside the scope of this study.

For the singular case, the forcing predictions obtained using RBE and RESPOD differ in the silent forcing components. RBE, by construction, predicts zero forcing in these components, while RESPOD captures the correlated information between the first and fourth components, and the fifth component, which is uncorrelated with the response, tends to zero. In a more complicated system, involving turbulent flow for example, this additional information obtained from RESPOD may be expected to provide additional insight regarding the mechanisms that underpin the forcing.

Note that although the SPOD modes are unit vectors in the Euclidean norm, the associated forcing modes obtained using RESPOD or RBE are not unit vectors. In (2.23), we see that the RESPOD mode is normalised using the response eigenvalue, so a unit norm is not ensured. Similarly, (2.11) implies that for a unit SPOD vector, the associated forcing mode obtained using RBE is not necessarily a unit vector. The norm of the forcing mode obtained by RBE/RESPOD is related by the associated gain. In RBE, amplified forcing modes will have a smaller-than-unity norm, such that $R\phi$ will be unity. In RESPOD, besides the associated gain, the norm also depends on the correlated-but-silent parts.

3. Identifying wall-attached structures and their forcing in turbulent channel flow

We use the tools outlined above to analyse turbulent channel flow, our objective being to educe, from DNS data, wall-attached structures and the forcing by which they are driven. We investigate if these wall-attached structures are reminiscent of attached eddies discussed widely in the literature.

Attached eddies begin to dominate the one-dimensional energy spectrum of a wall-bounded flow only beyond a certain value of *Re* ($Re_\tau \sim 100\,000$) (Perry *et al.* 1986; Chandran *et al.* 2017). But it has been shown that structure-eduction techniques can be used to identify such structures at lower *Re*: structure functions were used by Davidson *et al.* (2006*a*,*b*) and Agostini & Leschziner (2017), while Hellström *et al.* (2016) and Hellström & Smits (2017) used POD. In our study, we analyse structures that are correlated to the wall shear in a turbulent channel flow at $Re_\tau = 543$, our objective being to establish: (1) if these exhibit self-similar features consistent with attached eddies; and (2) if the associated forcing, identified using both RBE and RESPOD, also exhibits a self-similar organisation. The underlying aim is to lay the groundwork for a resolvent-based dynamic attached-eddy model, as discussed in the Introduction.

In the work of Yang & Lozano-Durán (2017), wall shear in the flow direction was shown to manifest self-similarity along the log layer, reminiscent of attached eddies, and this was used to build a model for momentum cascade. Here, we use instead the wall shear in the spanwise direction as the reference quantity to detect wall-attached structures. Our attempt to use the streamwise wall shear did not yield clear self-similarity in the associated coherent structures, and thus is not reported here.

3.1. *Database and definitions*

The flow data are provided by DNS of the incompressible Navier–Stokes equations using the 'ChannelFlow' code (see www.channelflow.ch for details). The DNS details are provided in table 1, where T_{max} and Δt denote the total simulation time and the time step, respectively, and $L_{x/y/z}$ and $N_{x/y/z}$ denote the domain and the grid size, respectively; the superscript $+$ denotes a near-wall unit. For dealiasing, a larger number of Fourier modes (3/2 times N_x and N_z) was used in the simulations. The subscripts *x*, *y* and *z* denote the streamwise, wall-normal and spanwise directions, respectively. The mean velocities and the root-mean-square values of the DNS data used were compared against the literature (del Álamo & Jiménez 2003) in Morra *et al.* (2021), and are therefore not presented here. To show the statistical convergence of the simulation, we check the balance in the mean momentum equation given as

$$0 = \frac{1}{Re_\tau} + \frac{\mathrm{d}^2 U_x^+}{\mathrm{d}y^{+2}} - \frac{\overline{uv}^+}{\mathrm{d}y^+}, \tag{3.1}$$

where U_x denotes the mean streamwise velocity, *u* and *v* denote the velocity fluctuations in the streamwise and wall-normal directions, respectively, an overbar indicates temporal averaging, and the superscript $+$ denotes quantities in wall units (see Wei *et al.* (2005) for further details). Integrating (3.1) in y^+ yields

$$-y = \frac{\mathrm{d}U_x^+}{\mathrm{d}y^+} - \overline{uv}^+. \tag{3.2}$$

The terms in (3.2) are plotted in figure 1, where it is seen that the summation of $\mathrm{d}U_x^+/\mathrm{d}y^+$ and $-\overline{uv}^+$ satisfies (3.2), hence the momentum balance is reached.
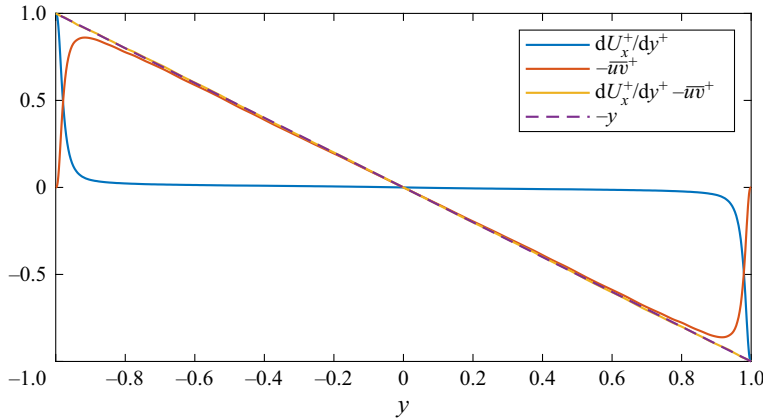
Figure 1. Momentum budget plot for the DNS of the channel flow.

Re_τ	Re_{bulk}	T^+_{max}	Δt^+	$L_x \times L_z$	$N_x \times N_y \times N_z$	Δx^+	Δz^+	Δy^+_{min}	Δy^+_{max}
543	10 000	8.84×10^3	2.95	$2\pi \times \pi$	$384 \times 257 \times 384$	8.88	4.44	4.09×10^{-2}	6.66

Table 1. Details of the DNS database.

The Fourier realisations are calculated using 128 fast Fourier transform (FFT) points with 80 % overlap between successive time blocks. The second-order exponential windowing function given in Martini *et al.* (2019) is used to perform the Fourier transform. The forcing correction associated with the windowing function is added to the Fourier realisations of the forcing as described in Martini *et al.* (2019) to ensure that the forcing and the response are related accurately to each other via the resolvent operator, as shown by Morra *et al.* (2021) and Nogueira *et al.* (2021).

The resolvent framework for incompressible isothermal viscous flows is given as follows. Defining $u_{tot} = U + u$ and $p_{tot} = P + p$ – where $U = [U_x, 0, 0]^T$ and $u = [u, v, w]^T$ are the mean and fluctuation velocities, respectively, defined in Cartesian coordinates ordered in streamwise, wall-normal and spanwise directions, and P and p are the mean and fluctuating pressure – the governing equations for momentum fluctuations are given as

$$\partial_t u + (U \cdot \nabla)u + (u \cdot \nabla)U = -\nabla p + \frac{1}{Re}\nabla^2 u + b + f, \\ \nabla \cdot u = 0, \left.\right\} \tag{3.3}$$

where $Re = U_{bulk}h/\nu$ denotes the Reynolds number, ν is the molecular viscosity, $f = -(u \cdot \nabla)u$ and $b = -\nabla P + Re^{-1}\nabla^2 U - (U \cdot \nabla)U$. Spatial derivative operators are given as $\nabla = [\partial_x, \partial_y, \partial_z]^T$ and $\nabla^2 = \nabla \cdot \nabla$. Defining the state vector $q = [u, v, w, p]^T$, and taking the Fourier transform in all homogeneous dimensions (x, z and t) with the ansatz $\hat{q}(\alpha, y, \beta, \omega) \exp(i(\alpha x + \beta z - \omega t))$, the governing equations given in (3.3) can be written in matrix form as

$$i\omega M\hat{q} - A\hat{q} = B\hat{f}, \tag{3.4}$$

considering that ω, α and β are not simultaneously zero, such that the b term, which varies only in y, has no contribution. Note that taking the Fourier transform in x and z allows an accurate and inexpensive explicit construction of the resolvent operator using pseudo-spectral methods.

Defining the transformation matrix $\hat{u} = C\hat{q}$, we can write (3.4) in resolvent form as

$$\hat{u} = R\hat{f}, \tag{3.5}$$

where $R = C(-i\omega M - A)^{-1}B$, and a hat denotes a Fourier-transformed variable. The matrices A, B, C and M are given in explicit form in Appendix A.

To investigate the wall-attached structures, we will define a measurement matrix

$$\tilde{C} = [0\ 0\ \partial_z|_{y=0}\ 0], \tag{3.6}$$

which yields, when we left-multiply it with (3.5),

$$\tau_z = \tilde{C}R\hat{f}, \tag{3.7}$$

where $\tau_z = \partial_z w|_{y=0}$ is the spanwise wall shear. We choose to measure τ_z considering that it is strongly associated to quasi-streamwise vortices. We then apply the RESPOD to obtain the forcing that is correlated with the wall shear. Note that since τ_z is a scalar quantity, it has one SPOD mode that is also scalar, and the associated forcing is bound to be rank-1, which yields

$$\psi = \tilde{C}R\chi. \tag{3.8}$$

The RESPOD mode χ, when multiplied with the resolvent operator R, yields the velocity field that is correlated with τ_z. The proof is provided in the following. Using the velocity vector $\hat{u}$ as the target event in (2.23) instead of the forcing $\hat{f}$, one can obtain the velocity field ξ that is correlated with τ_z as

$$\xi = \frac{E\{\hat{u}a^H\}}{\lambda}, \tag{3.9}$$

where, for the particular case of τ_z being a scalar, $a = \langle \tau_z, 1 \rangle$ and the eigenvalue λ is obtained simply by $E\{\tau_z \tau_z^H\}$. Substituting (3.5) into (3.9) gives

$$\xi = R\chi, \tag{3.10}$$

which proves the above statement. Since ξ, also rank-1, corresponds to all and the only parts in $\hat{u}$ that are correlated with τ_z (see the discussion in § 2.2 or alternatively Borée (2003)), we consider it as the wall-attached part of $\hat{u}$.

3.2. *Power spectral densities*

The DNS database is decomposed into Fourier modes in streamwise and spanwise directions. In figure 2, we show the power spectral density (PSD) of τ_z at different α^+ and β^+ values. Peak energy location is seen to move towards higher ω and β for increasing α while the amplitude reduces. Attached eddies are expected to be the main energy-containing structures in the flow (Townsend 1976) and exhibit a self-similar organisation. Self-similarity implies that structures in the same hierarchy should have constant streamwise-to-spanwise and streamwise-to-wall-normal ratios. In a flow database that is decomposed into Fourier modes in the streamwise and spanwise directions,
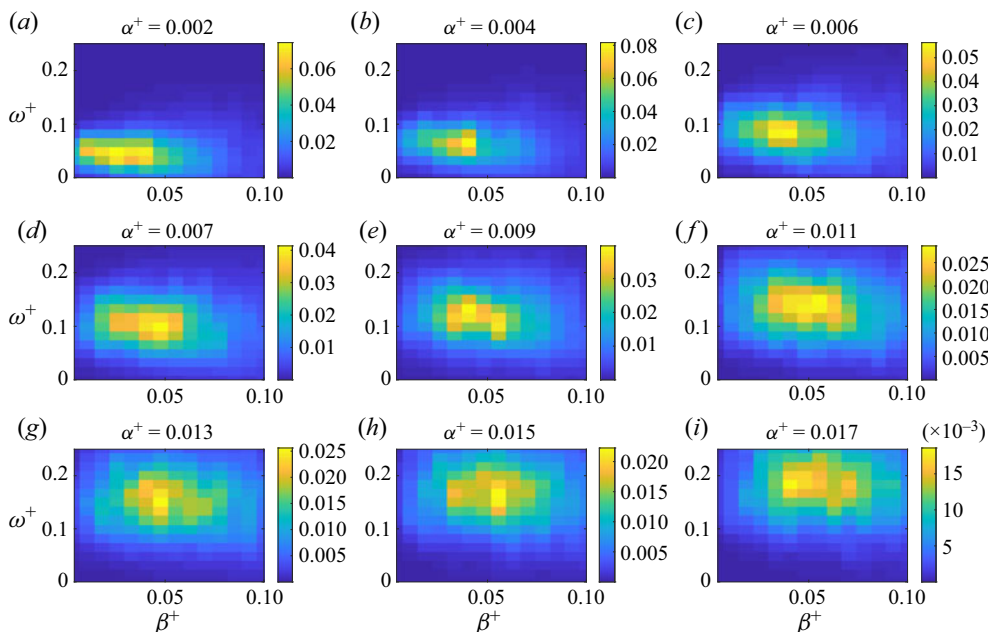
Figure 2. PSD map of τ_z for different α^+ values.

self-similarity can be investigated by imposing it in the horizontal plane by fixing the streamwise-to-spanwise aspect ratio (AR) and searching for it in the wall-normal direction, similar to Hellström *et al.* (2016) and Hellström & Smits (2017). In what follows, we first set $\lambda_x^+/\lambda_z^+ = 6$, where λ_x and λ_z are the streamwise and spanwise wavelengths, and look for self-similar structures at this AR. We then extend our analysis to a range of ARs and provide an overall view of self-similarity for the given channel flow. We first investigate self-similarity of structures at frequencies with high spectral energy, which is followed by investigation of self-similarity in less energetic structures.

Maximum-energy-containing frequency ω_{max} for different α^+ values with AR = 6 is shown in figure 3. We see that ω_{max} increases almost linearly with α^+. We approximate this trend with the red line shown in the figure, which is the best linear fit minimising L_1-norm error. The L_1-norm is chosen for the trend line to be less sensitive to outliers. The frequency corresponding to each $(\lambda_x^+, \lambda_z^+)$ pair is selected using this trend line.

The accuracy of the forcing database in $Re_\tau = 543$ flow is verified by comparing the state $\hat{q}$ to its resolvent-based prediction $\boldsymbol{R}\hat{f}$ in figure 4. Such an evaluation has already been performed by Morra *et al.* (2021) for two dominant structures, and it is here extended to a broader range of wavenumbers. As seen in the figure, the resolvent-based prediction of the response matches the DNS state data for the entire wavenumber span considered.

The square root of PSD of the wall shear τ_τ calculated at ω_{max} is shown in figure 5. The amplitude is seen to decrease for increasing α^+ as expected from figure 2. The trend is almost linear for $\alpha^+ > 7.4 \times 10^{-3}$.

3.3. *Wall-attached coherent structures and associated forcing for AR = 6*

We now focus on the wall-attached structures at the peak-energy frequency, ω_{max}^+, for each $(\lambda_x^+, \lambda_z^+)$ pair with AR fixed at 6. The modes are forced to be symmetric in u and
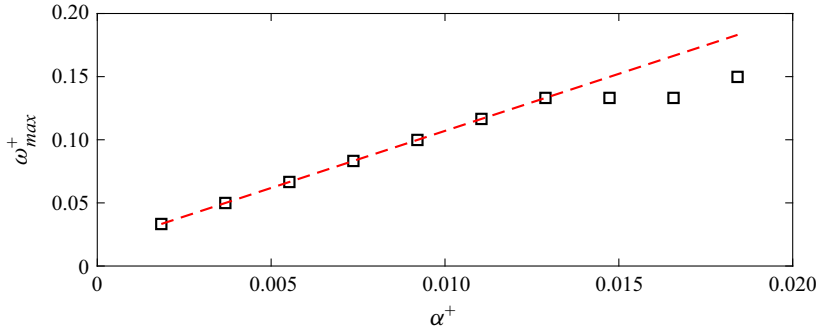
939 A36-14

Figure 3. Maximum-energy-containing frequency, ω_{max}, of spanwise wall shear τ_z for different Fourier-mode pairs with AR = 6. The red dashed line indicates the best fit minimising L_1-norm error.
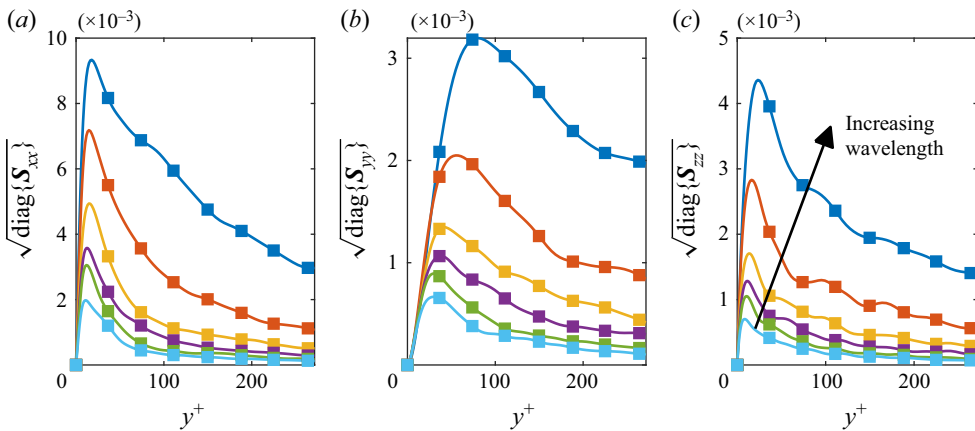

Figure 4. PSD of the response $\hat{q}$ (solid lines) in comparison to its resolvent-based prediction $\boldsymbol{R}\hat{f}$ (markers) at ω_{max} for different Fourier-mode pairs with AR = 6. Wavelengths plotted are $\lambda_x^+ = 487$, 569, 683, 853, 1137 and 1706.

w (and anti-symmetric in v) about the channel centre in the wall-normal direction by averaging the flow fields in the bottom and the upper halves of the channel (considering a minus sign in v), as in Abreu *et al.* (2020a). In figure 6, wall-shear-associated forcing modes obtained using RESPOD and RBE methods, respectively, and the velocity fields generated by these forcing modes, are shown. Note that the mode amplitudes are adjusted to have unit wall shear. The forcing from the RBE method, $\boldsymbol{\phi}$, shows that the spanwise and wall-normal components of forcing drive the wall-shear dynamics observed in the flow at this AR, while the streamwise component is almost not required. For the forcing from the RESPOD method, $\boldsymbol{\chi}$, on the other hand, the forcing mechanisms that generate wall shear involve to a large extent the streamwise component of forcing, although its overall contribution to wall-shear dynamics can be small, as suggested by the RBE results. This indicates strong cancellations among the responses to different forcing components, similar to the results in Morra *et al.* (2021). This will be investigated further at the end of this subsection. As discussed earlier, the response $\boldsymbol{\xi} = \boldsymbol{R}\boldsymbol{\chi}$ yields the velocity field associated with the wall shear. Similarly, $\boldsymbol{R}\boldsymbol{\phi}$ can be interpreted as best prediction of the correlated velocity field when no data for forcing are available. This amounts to flow estimation using low-rank measurements with the assumption of forcing CSD $\boldsymbol{P} = \boldsymbol{I}$, as
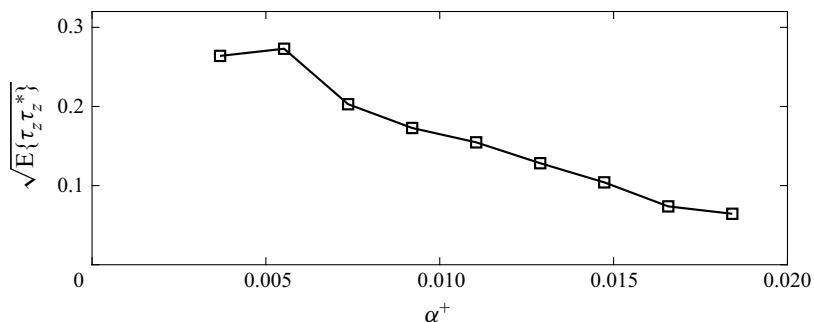
Figure 5. Amplitude spectral density of spanwise wall shear τ_z at ω_{max} for different Fourier-mode pairs with AR = 6.
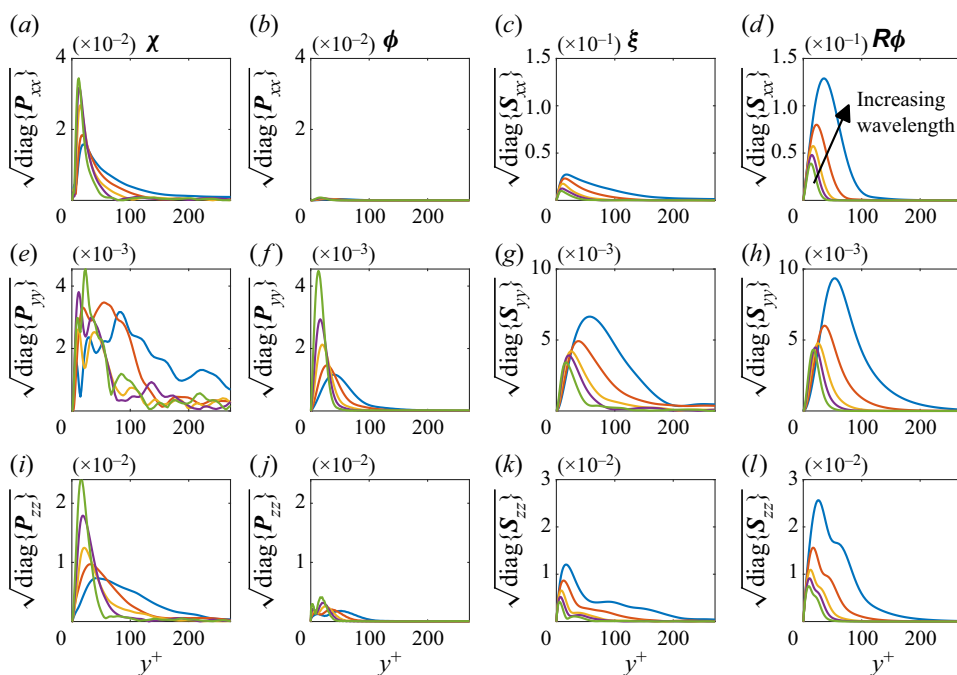

Figure 6. Comparison of the wall-shear-associated forcing modes obtained by RESPOD (a,e,i) and RBE (b,f,j), and the corresponding velocity fields ((c,g,k) and (d,h,l), respectively), at $\lambda_x^+ = 341, 487, 682, 1137$ and 1706, with $\lambda_x^+/\lambda_z^+ = 6$.

discussed in Martini *et al.* (2020). We see that the velocity modes associated with the wall shear are significantly overpredicted when RBE is used.

As mentioned above, the difference between the minimal-norm forcing $\boldsymbol{\phi}$ and the wall-shear-correlated forcing $\boldsymbol{\chi}$ implies that contributions to τ_z from each component of $\boldsymbol{P_\chi} = \boldsymbol{\chi}\boldsymbol{\chi}^H$ cancel each other to a significant extent. To understand the effect of a particular component of $\boldsymbol{\chi}$ (or $\boldsymbol{\phi}$), we calculate the wall shear using $\boldsymbol{\chi}$ (or $\boldsymbol{\phi}$) with that component masked. The resulting wall-shear PSDs for partially masked $\boldsymbol{\chi}$ and $\boldsymbol{\phi}$, respectively, are shown in figure 7. The forcing modes are scaled such that using the full forcing mode generates a wall shear with unit amplitude at each wavenumber pair. For the wall-shear-correlated forcing $\boldsymbol{\chi}$, we see that the wall-normal component has the least

939 A36-16
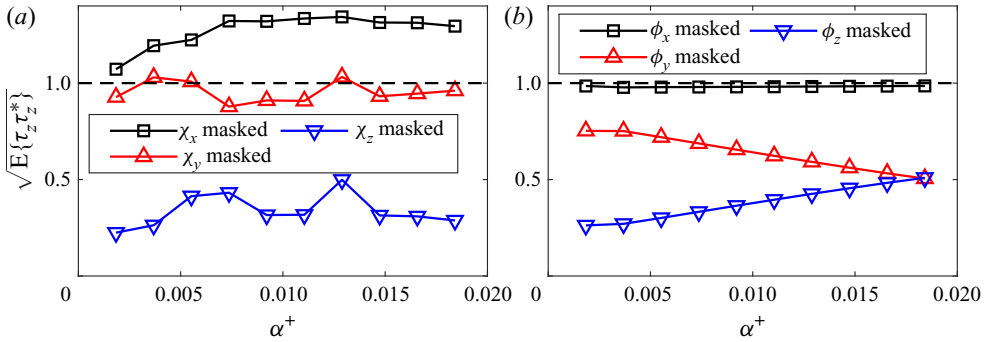
Figure 7. Square root of PSD of τ_z obtained using partially masked $\boldsymbol{\chi}$ (*a*) and $\boldsymbol{\phi}$ (*b*) at different wavenumbers, with AR = 6. Unmasked PSDs are all unity, shown by the dashed lines.

effect on the resulting τ_z amplitude at every wavenumber pair. In the case of minimal-norm forcing $\boldsymbol{\phi}$, on the other hand, the streamwise component has negligible effect on wall-shear dynamics. This implies that the mechanisms involved in the two forcing modes are indeed different, although amounting to the same overall response. For $\boldsymbol{\phi}$, wall shear is generated by a pure streamwise vortical forcing at every wavenumber. For $\boldsymbol{\chi}$, it is the streamwise and spanwise components that are important, with the latter being the main driving component. This implies that turbulence does not follow the optimal path to generate wall-shear fluctuations. The fact that masking χ_x increases $\sqrt{\mathrm{E}\{\tau_z\tau_z^*\}}$ implies that simultaneous presence of the streamwise and spanwise components causes some cancellation in the wall-shear fluctuation amplitude.

   Note that the predictions from the RBE method can be improved using an eddy-viscosity model. The eddy viscosity is often used to enhance modelling properties of the resolvent operator (Morra *et al.* 2019; Pickering *et al.* 2019). It was used in Towne *et al.* (2020) and was more effective to recover flow (*q*) statistics. As shown in Morra *et al.* (2021), the eddy viscosity embeds some of the forcing statistics in the resolvent operator, but not all (Amaral *et al.* 2021). A drawback of using eddy viscosity is that the forcing of an eddy-viscosity-based resolvent operator does not correspond to the actual nonlinear Navier–Stokes terms. Since we are interested in these nonlinear terms, we use the molecular-viscosity-based resolvent operator, as it allows us to probe directly the nonlinear terms via the forcing $\boldsymbol{f}$.

3.4. *Self-similarity of wall-attached forcing and response structures for AR = 6*

Townsend's AEH states that the attached eddies scale in size with respect to their distance to the wall (Townsend 1976; Perry & Chong 1982). We will assess the validity of this assumption for the wall-attached structures investigated in this study. As mentioned earlier, by keeping the AR fixed, we impose self-similarity in the streamwise and spanwise directions. Regarding the modes seen in figure 6, although the amplitudes show different trends, particularly for different forcing components, we see that the mode shapes exhibit to a certain extent a self-similar trend, except for the wall-normal component of the forcing mode $\boldsymbol{\chi}$. The self-similarity can be made apparent by a proper scaling of the modes in the wall-normal direction and normalisation of each mode with its peak amplitude. To assess the self-similarity in the wall-normal direction, Hellström *et al.* (2016) proposed a scaling based on the peak of the POD modes. In a similar spirit, we propose a scaling based on
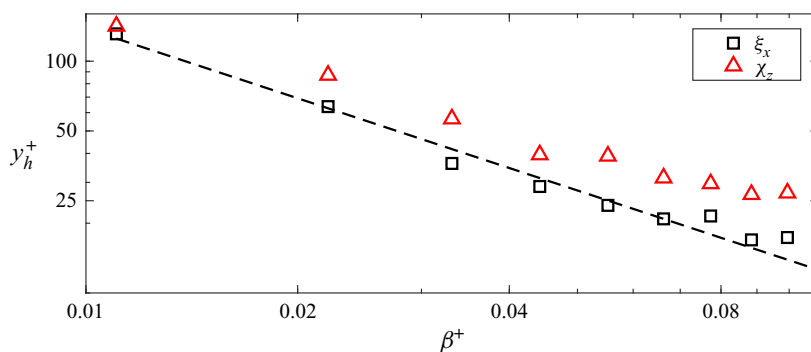
Figure 8. Mode centre y_h^+ obtained using ξ_x (square) and χ_z (triangle) at different wavenumbers, with AR = 6. The dashed line shows the $1/\beta^+$ trend.

the integral function

$$g(\alpha, y) = \int_0^y |\xi_x(\alpha, y, \beta(\alpha), \omega_{max}(\alpha))|\, \mathrm{d}y, \tag{3.11}$$

where ξ_x is the streamwise component of the wall-shear-correlated velocity mode $\boldsymbol{\xi}$, and we use this function to define a characteristic length scale y_h such that $g(\alpha, y_h) = g(\alpha, H)/2$, where H is the channel half-height. In other words, $y_h(\alpha)$ is the wall-normal position that divides the area under $|\xi_x|$ into two equal parts. The β^+ dependence of y_h^+ is shown in figure 8. We repeat this analysis with χ_z instead of ξ_x and show the results in the same figure. The component χ_z is chosen as it is the dominant component in generating wall shear, as shown in figure 7. Consistent with the attached-eddy hypothesis (Townsend 1976; Perry & Chong 1982), the wall-attached structures with the same AR computed at the peak-energy frequency, ω_{max}, follow a β^{-1} trend except for the very small scales ($\beta^+ > 0.09$). The forcing modes also follow a similar trend, which again deviates from β^{-1} at small scales. The wall-attached structures scaling with β^{-1}, consistent with the AEH, suggests a self-similar behaviour. The forcing modes following a similar trend suggests that the mechanisms that generate these structures may also be self-similar, i.e. dynamic self-similarity in addition to Townsend's kinematic self-similarity.

The characteristic eddy length scale, y_h, can now be used to normalise the structures seen in figure 6. We reconstruct the forcing and response modes in the y–z plane, which corresponds to channel cross-section. Mode phases at each $(\lambda_x^+, \lambda_z^+)$ pair are shifted to have $\angle\tau_z = 0$. We use y_h based on ξ_x to scale both the forcing and response modes in the y- and z-directions. We normalise the wall-normal and spanwise components of both forcing modes, $\boldsymbol{\chi}$ and $\boldsymbol{\phi}$, with χ_x, and similarly those of the response modes with ξ_x. The reconstructed modes, shown in figure 9, reveal self-similarity of the wall-attached structures and the associated forcing. The streaks and the streamwise vortices seen in the response modes $\boldsymbol{\xi}$ indicate that the wall shear τ_z is associated with the lift-up mechanism (Brandt 2014). As discussed earlier, the RBE method overpredicts the wall-shear-correlated velocity field. The modes are once again reminiscent of the lift-up mechanism, with the streaks and the streamwise vortices considerably more tilted in the spanwise direction. The optimal forcing $\boldsymbol{\phi}$, which is sufficient to create the wall shear observed in the flow, has a streamwise-vortex-like structure. This is consistent with the optimal forcing modes in Couette flow discussed in Hwang & Cossu (2010a). The forcing
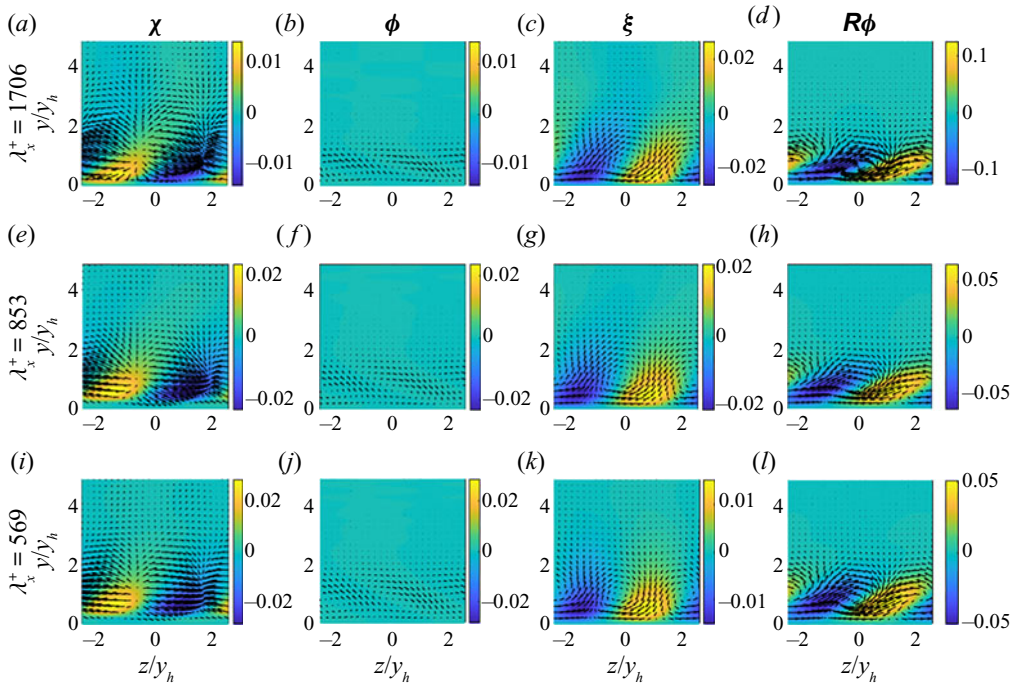
939 A36-18

Figure 9. Reconstruction of wall-shear-associated forcing modes χ (a,e,i) and ϕ (b,f,j), and the corresponding velocity fields ((c,g,k) and (d,h,l), respectively) in the y–z plane at three wavenumbers (from top to bottom). Colour plots indicate the x-component, while vectors show y- and z-components. The domain is rescaled using y_h for each wavenumber.

modes that actually take place in the flow, on the other hand, do not reveal immediately such a simple structure, although showing self-similarity in itself.

3.5. *Extension of self-similarity analysis to other ARs*

Given the self-similarity observed at the wall-attached structures with $AR = 6$, we now extend our analysis to other ARs ranging from 2 to 10. Once again we look for the dominant structures extracted by choosing the maximum-energy-containing frequency for each (λ_x^+, λ_z^+) pair for a given AR. Figure 10 shows the peak-energy frequency ω_{max}^+ versus wavenumber plots for different ARs, together with the linear trends minimising L_1-norm error. We see that all the trends for different ARs collapse onto the same line, given by $\omega^+ = 9.04\alpha^+ + 0.0166$. We use this linear trend to set the frequency for a given (λ_x^+, λ_z^+) pair at a given AR.

We calculate the mode centre y_h and investigate its change with respect to the spanwise wavenumber β. Similar to the analysis conducted for the $AR = 6$ case, we compute y_h using ξ_x and χ_z, respectively, and show the results for different ARs in figure 11. Overall, we observe the β^{-1} trend for both the response and forcing structures at every AR, which imply that self-similarity may be present for all the dominant wall-attached structures and the associated forcing for a broad range of ARs. In general, the small-scale structures near the wall are seen to deviate from the β^{-1} trend for all the ARs. This deviation may be due to increasing viscous effects at this region. We see that at certain ARs, the largest forcing
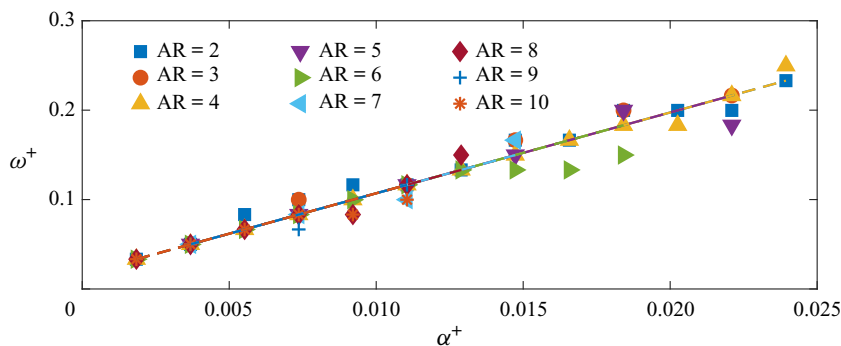
Figure 10. Peak-energy-containing frequencies for different wavenumber pairs with fixed AR. Different markers indicate different AR values. The coloured dashed lines correspond to the best-fit lines for different ARs, using the same colour code.
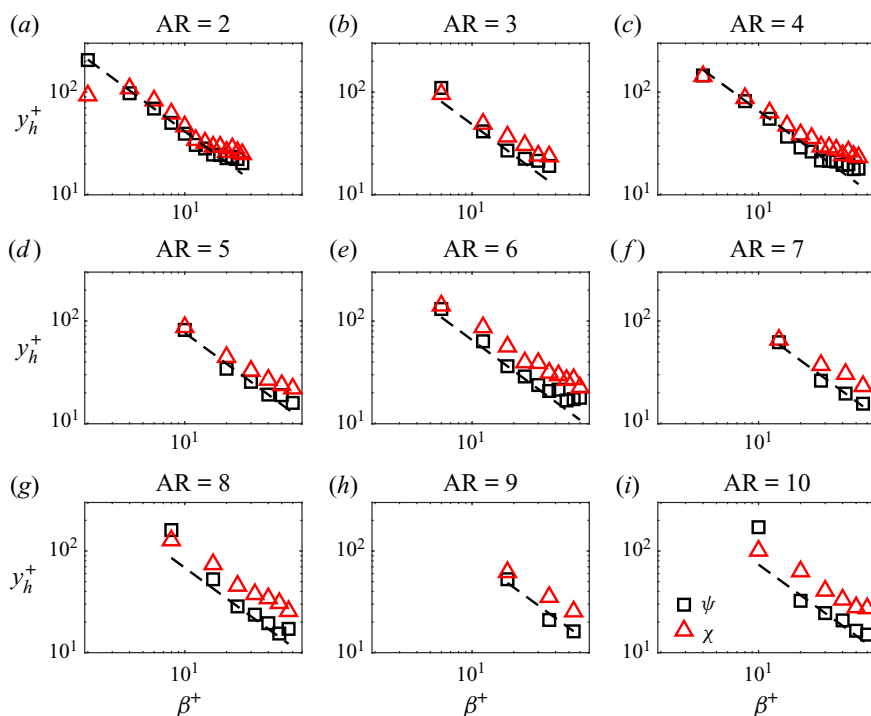

Figure 11. Mode centre y_h^+ obtained using ξ_x (square) and and χ_z (triangle) at different wavenumbers. Each subplot shows results for a different AR. The dashed lines show the $1/\beta^+$ trends.

and/or response structures also deviate from the β^{-1} trend. This may be caused by these structures being affected by the other half-channel at the given *Re*.

To quantify self-similarity, we define the following measure. Given ζ as any component of any response or forcing mode for a given $(\lambda_x^+, \lambda_z^+)$ pair at a given AR, we first normalise ζ with its peak value, given as ζ_n, and then perform y_h scaling as

$$\zeta_n(y) = \tilde{\zeta}_n(y/y_h), \tag{3.12}$$

to get ζ_n in self-similar coordinates, where y_h is calculated using ξ_x. After performing this analysis for all the wavenumber pairs at a given AR, we find the 'mean' self-similar mode by averaging these modes as

$$\mathrm{E}\{\tilde{\zeta}_n\} = \frac{1}{N} \sum_i^N \tilde{\zeta}_n^{(i)}, \tag{3.13}$$

where N denotes the total number of wavenumber pairs at that AR. We then compute the alignment of $\tilde{\zeta}_n^{(i)}$, which corresponds to the ith wavenumber pair, with this mean self-similar mode as

$$\gamma_\zeta^{(i)} = \frac{|\langle \tilde{\zeta}_n^{(i)}, \mathrm{E}\{\tilde{\zeta}_n\}\rangle|}{\sqrt{\langle \tilde{\zeta}_n^{(i)}, \tilde{\zeta}_n^{(i)}\rangle}\sqrt{\langle \mathrm{E}\{\tilde{\zeta}_n\}, \mathrm{E}\{\tilde{\zeta}_n\}\rangle}}. \tag{3.14}$$

According to (3.14), $\gamma_\zeta^{(i)}$ becomes 1 in case of perfect self-similarity, and 0 in case of no self-similarity. Assuming that a self-similar behaviour is present in all the data considered, the averaging process will clearly reveal the self-similar profile, with each data point showing small deviations from it. Note, however, that if self-similar behaviour is found in only a limited range of parameters, e.g. λ_z, then including data points outside this range can mask the self-similar behaviour. That is, the approach used is prone to false negatives, being a conservative identification method.

In figure 12, we show the similarity maps γ_χ, γ_ϕ and γ_ξ for different ARs and α^+ values. White regions in the figure correspond to wavenumber pairs that are not contained in the database. In general, as all the modes have similar phase and the mode shapes are never too different from each other, for almost all the cases the self-similarity coefficient given in (3.14) takes values close to 1. However, we observed by visual inspection that self-similarity is sufficiently clear only for $\gamma > 0.9$. Therefore, we set this as the lower limit in the maps shown in figure 12. The wall-attached structures given by ξ show strong self-similarity except the very-large-scale structures, which, once again, potentially are affected by the other half-channel. We see a slight reduction in the self-similarity of the smallest scales, particularly in the wall-normal and spanwise velocity components, ξ_y and ξ_z, respectively. This reduced self-similarity is in agreement with the deviation of the small-scale structures from the β^{-1} trend as shown in figure 11.

Parallel to the wall-attached structures, the associated minimal-norm forcing, ϕ shows also self-similarity, although slightly reduced, in all its components except the large-scale structures. Note that the minimal-norm forcing ϕ involves only the response and the resolvent operator. Given that the response is self-similar, this result implies that the resolvent operator induces self-similarity as well. This is in line with the findings of Hwang & Cossu (2010*a*), McKeon (2017) and Sharma *et al.* (2017).

Regarding the wall-shear-correlated forcing χ, we observe self-similarity in the streamwise and spanwise components, χ_x and χ_z, respectively, with that in χ_z being slightly higher. No such self-similarity is seen in the wall-normal component χ_y. A potential reason for that may be the lower amplitude of forcing modes in the y-direction compared to other components, as illustrated in figure 6; statistical convergence for low-amplitude components is sufficiently harder, as χ_y is the smallest and the least effective forcing component in terms of wall-shear dynamics (see figure 7). Even being limited to χ_x and χ_z, given that wall shear is determined mainly by these components, the self-similarity seen in χ implies self-similar mechanisms associated
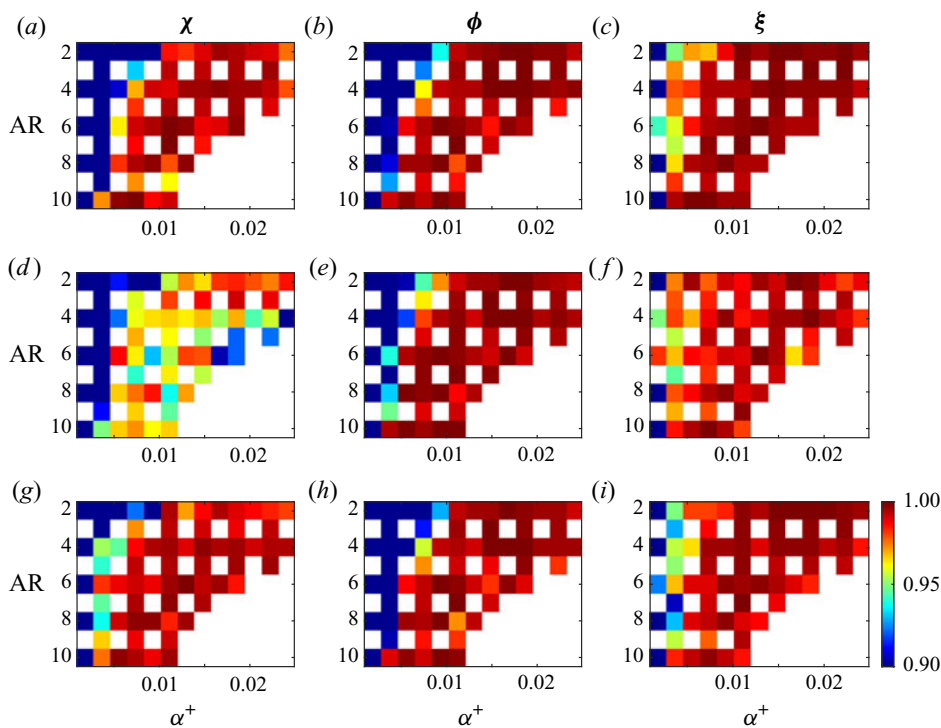
Figure 12. Self-similarity maps γ_χ (a,d,g), γ_ϕ (b,e,h) and γ_ξ (c,f,i), for different ARs and α^+ values. Panels (a–c), (d–f) and (g–i) correspond to the x-, y- and z-components, respectively.

with the wall-attached structures. The presence of such self-similar mechanisms may be beneficial for modelling wall-shear dynamics and attached eddies.

The mean self-similar modes of forcing and response for different ARs are shown in figure 13. The streamwise and wall-normal response components, ξ_x and ξ_y, respectively, have similar mode shapes for all ARs. The spanwise component has a double-peak structure, becoming more apparent with increasing AR, which implies that the streamwise vortex, and the lift-up mechanism, become more evident at higher AR. The double-peak in the spanwise component of the minimal-norm forcing ϕ_z seen at every AR indicates that the optimal forcing for wall shear always has a vortex-like structure. We do not see such a structure in the correlated forcing χ. Note that the correlated forcing contains both solenoidal and non-solenoidal parts, which may result in disappearance of the vortex shape. A similar observation was reported in Morra *et al.* (2021).

The similarity analysis provided in this subsection involves only the mode shapes, ignoring any amplitude information. To investigate the trends in the mode amplitudes, we plot also the peak values for the absolute value of each mode component in figure 14, this time without normalising the modes to have unit wall shear. We see in figure 14 that mode amplitudes of correlated velocity decay with constant power with increasing β^+, with the decay rate being ~2. The only exception is at AR $= 2$, which is shown in red. The decay rate is nearly the same for all three components at all ARs from 3 to 10. Mode amplitude increases up to AR $= 6$, and then saturates. In the minimal-norm forcing ϕ, the amplitude of the streamwise component is seen to be an order of magnitude smaller than the spanwise component. The amplitude difference increases with AR: ϕ_x becomes smaller, while

939 A36-22
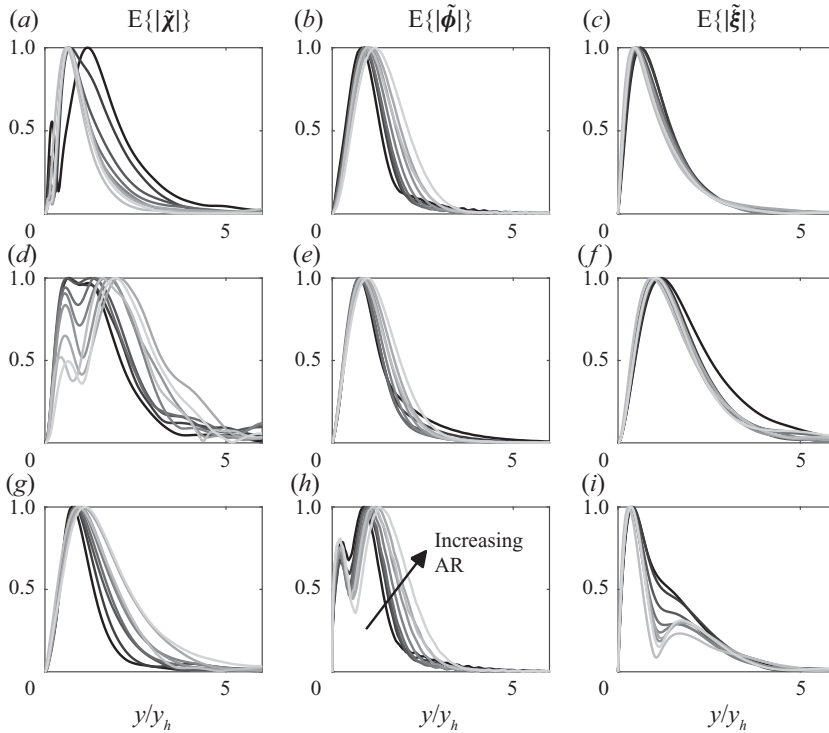
Figure 13. Mean self-similar modes for $\boldsymbol{\chi}$ (a,d,g), $\boldsymbol{\phi}$ (b,e,h) and $\boldsymbol{\xi}$ (c,f,i). Panels $(a$–$c)$, $(d$–$f)$ and $(g$–$i)$ correspond to the x-, y- and z-components, respectively.

ϕ_z remains unchanged. Similar to the minimal-norm forcing, wall-normal and spanwise components of wall-shear-correlated forcing, χ_y and χ_z, respectively, have nearly the same amplitudes with increasing AR. The amplitude of the streamwise component χ_x, on the other hand, increases up to AR = 6 and saturates for higher AR, similar to the response mode.

3.6. *Self-similarity at sub-dominant wall-attached structures*

We will now investigate if the self-similarity observed in the dominant wall-attached structures extends to sub-dominant structures as well. To achieve this, we shift the trend line used to select the frequency for a given wavelength pair, as seen in figure 15. The ratio of the corresponding wall-shear spectra to that of the dominant structures investigated above is shown in figure 16. We see that when shifting to higher frequencies, the energy content at small wavenumbers drops significantly, while at high wavenumbers, it remains comparable to the energy in dominant structures.

We calculate mode centre y_h based on ξ_x for these sub-dominant structures, and investigate its change with β in figure 17. It is observed that the β^{-1} trend appears only at wavenumbers where τ_z contains energy at levels comparable to the dominant structures. Figure 18 shows the self-similarity maps γ_χ, γ_ϕ and γ_ξ for these sub-dominant structures, similar to figure 12. Consistent with the y_h versus β trends in figure 17, we observe self-similarity only at wavenumbers that contain high energy. The analysis was repeated for different shift values for ω, and similar results were obtained but are not presented
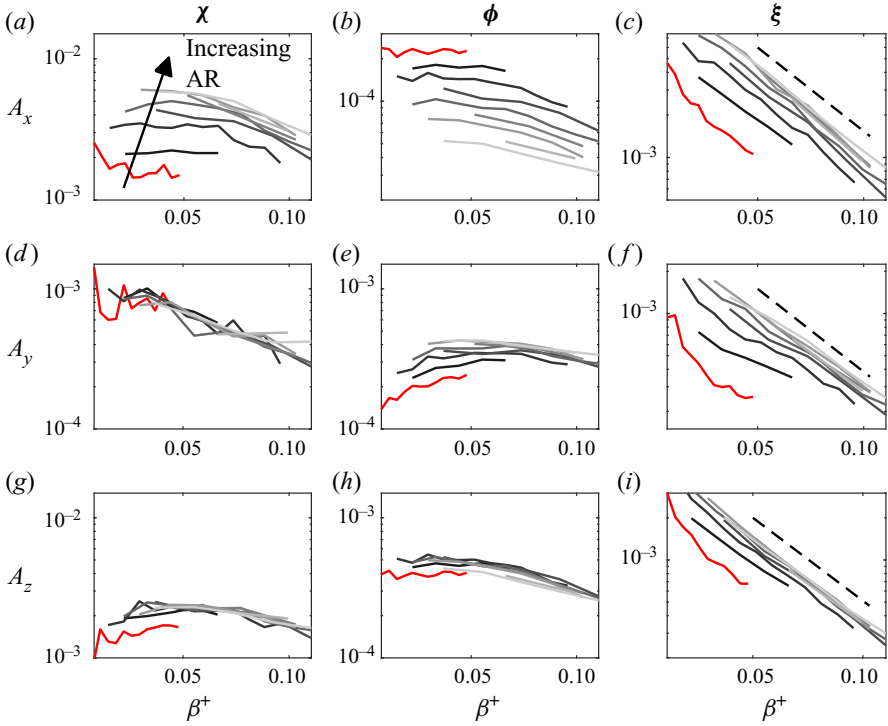
Figure 14. Mode amplitudes for χ (*a,d,g*), ϕ (*b,e,h*) and ξ (*c,f,i*) at different wavenumber pairs. Panels (*a–c*), (*d–f*) and (*g–i*) correspond to the *x*-, *y*- and *z*-components, respectively. ARs range from 2 to 10; AR = 2 is shown in red, and the rest with greyscale. Dashed lines indicate the $1/(\beta^+)^2$ trends.
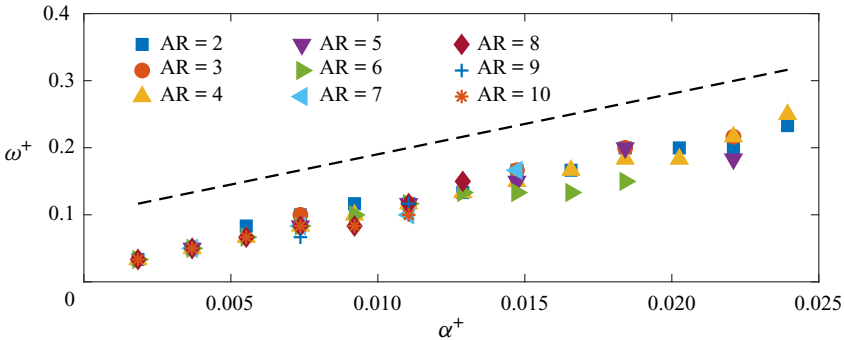

Figure 15. Shifted trend line for ω^+ corresponding to sub-dominant wall-shear structures.

here for brevity. These results imply that high-energy-containing wall-attached structures, even if sub-dominant, and the associated forcing show self-similarity at a wide range of wavenumbers and ARs. Parallel to the lack of self-similarity in the wall-normal component of the forcing, the reason for not observing self-similarity in the low-energy modes may once again be slower convergence rates for these modes.
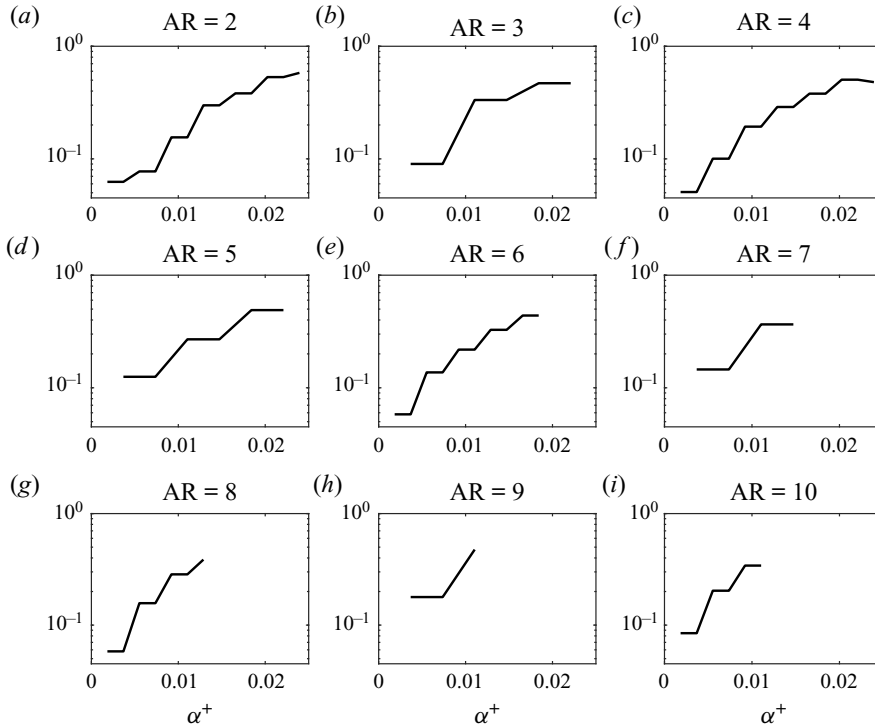
939 A36-24

Figure 16. Ratio of the amplitude of τ_z calculated at sub-dominant frequencies to that calculated at ω_{max} at different wavenumbers.

4. Conclusions

We investigated the self-similarity of wall-attached structures in turbulent channel flows with a view to identifying attached eddies in the boundary layer. A flow database, obtained by direct numerical simulations (DNS), is considered with Reynolds number $Re_\tau = 543$. The analysis is based on the attached-eddy hypothesis (AEH) (Townsend 1976; Perry & Chong 1982), which holds that attached eddies are high-energy-containing structures that dominate the logarithmic region of the boundary layer, and whose size is determined by their distance to the wall. Guided by this definition, we explore self-similarity by considering the wall-normal organisation of streamwise–spanwise Fourier-mode pairs associated with a fixed aspect ratio; we then identify flow structures and forcing modes associated with wall shear in the spanwise direction, τ_z. Spanwise wall shear was chosen as the representative quantity for quasi-streamwise vortices. The single-point measurement considered here amounts to a rank-1 system, which allows, within the linear framework provided by the resolvent analysis (Hwang & Cossu 2010*a*; McKeon & Sharma 2010; Cavalieri *et al.* 2019; Lesshafft *et al.* 2019), identification of the flow structure associated with the wall shear, i.e. wall-attached structures, and the associated forcing. We used resolvent-based spectral proper orthogonal decomposition (RESPOD) to perform an identification of wall-attached response and forcing modes. The method was compared to the resolvent-based estimation (RBE) approach of Towne *et al.* (2020), which yields the minimal-norm forcing to generate a given response. We observe that using a linear scaling between the frequency and the streamwise wavenumber, the resulting wall-attached structures exhibit self-similarity in line with the AEH for a wide range of wavenumbers and aspect ratios. The frequency scaling is determined regarding the linear trend observed
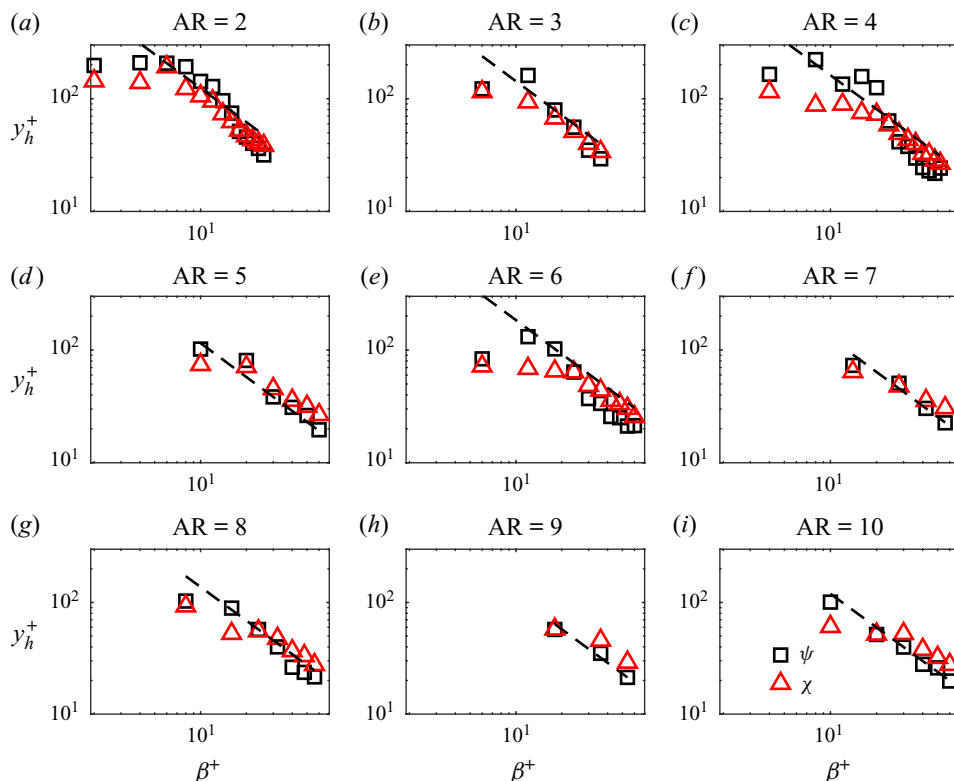
939 A36-25

Figure 17. Mode centre y_h^+ obtained using ξ_x (square) and and χ_z (triangle) at different wavenumbers at sub-dominant frequencies. Each subplot shows results for a different AR. The dashed lines show the $1/\beta^+$ trends.

in the peak frequency of the power spectral density (PSD) of τ_z with respect to the streamwise wavenumber. Keeping the slope of the linear scaling constant, we observe that self-similarity extends to structures at sub-dominant frequencies as well. Although we do not particularly seek energetic structures, it was shown in Cheng *et al.* (2020), where a number of turbulent channels (including one at $Re = 550$) were investigated, that the wall-attached structures are dominant regarding the energy that they contain. As we observe self-similarity in wall-attached structures in a wide range of frequencies and aspect ratios, we expect these structures to be relevant in terms of the AEH.

We extend the analysis to investigate such self-similarity for the forcing structures, again, associated with the wall-shear. Our findings reveal that both the minimal-norm forcing required to obtain the measured wall-shear dynamics (obtained by RBE) and the wall-shear-correlated forcing (obtained by RESPOD) that also drives the wall-attached flow structures exhibit self-similar behaviour.

The self-similarity of forcing modes obtained using RBE can be associated with the works of Hwang & Cossu (2010a), Moarref *et al.* (2013) and Sharma *et al.* (2017), among others, where it was shown that self-similarity is a property of the resolvent operator. Given the SPOD modes that are self-similar, it may be expected that associated forcing modes predicted by RBE would be self-similar. But the demonstration of a forcing self-similarity using the RESPOD approach illustrates how that self-similarity is indeed present in the actual forcing data, suggesting a self-similar organisation of the nonlinear
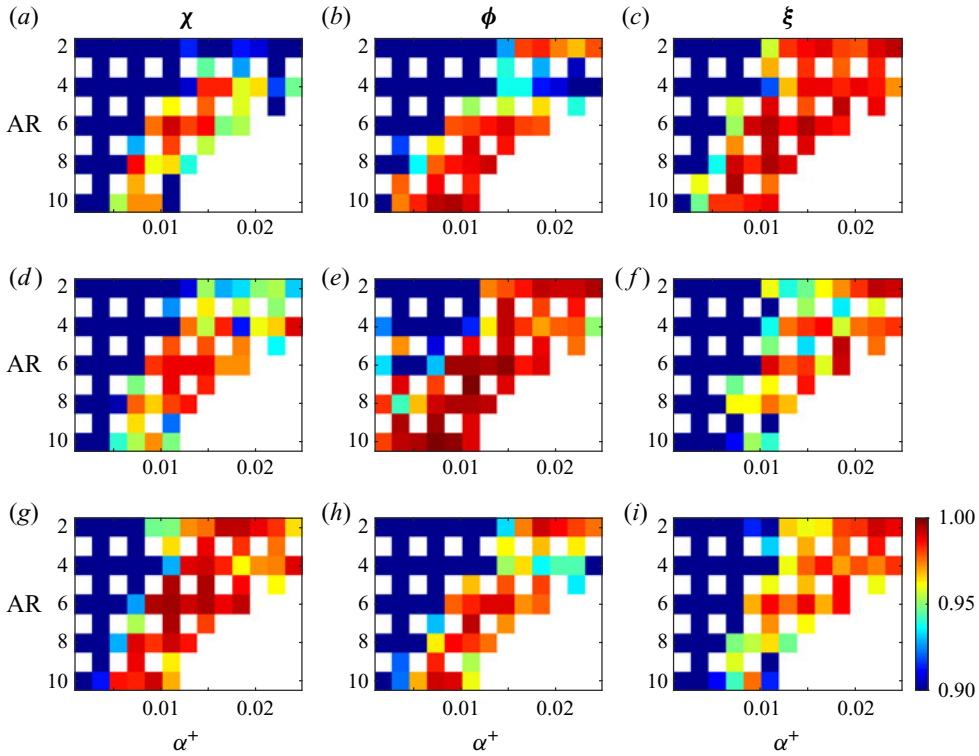
Figure 18. Self-similarity maps γ_χ (a,d,g), γ_ϕ (b,e,h) and γ_ξ (c,f,i), for different ARs and α^+ values, obtained at sub-dominant frequencies. Panels $(a–c)$, $(d–f)$ and $(g–i)$ correspond to the x-, y- and z-components, respectively.

scale interactions that drive attached eddies. The self-similar forcing structures are shown to lead to elongated streaky structures, which are sustained by the lift-up mechanism, consistent with the discussion of Cossu & Hwang (2017) in which streaks and streamwise vortices participate in the lift-up mechanism as two interconnected elements of a single attached eddy.

The self-similar forcing educed from the DNS data may be used to construct dynamical models of attached eddies, following ideas similar to the works of Moarref *et al.* (2013), Hwang & Eckhardt (2020) and Skouloudis & Hwang (2021). These works superpose coherent structures obtained with the linearised Navier–Stokes operator such that the overall Reynolds stresses are obtained. As presented in this work, RESPOD is an appropriate technique to obtain the forcing that is coherent with a given flow response. The observed self-similarity of the forcing modes may be included in dynamic models of attached eddies for improved predictions of flow properties.

Another promising direction is the use of the identified self-similar forcing to build flow estimators from a limited number of sensors. Linear estimators require assumptions of the forcing, and the quality of predictions depends on the accuracy of the forcing statistics included in the estimation (Chevalier *et al.* 2006; Martini *et al.* 2020; Amaral *et al.* 2021). For wall turbulence, the specification of a self-similar forcing may be a viable approach to construct accurate estimators, especially for high Reynolds numbers for which one cannot obtain DNS data.

U. Karban, E. Martini, A.V.G. Cavalieri, L. Lesshafft and P. Jordan

Studies of coherent structures in flows have benefited greatly from the analysis of the linearised Navier–Stokes operator, which, by its non-normality, leads to more amplified structures that are more likely observed in a turbulent flow. However, a more refined view is obtained if the actual nonlinear terms, which constitute a forcing in resolvent analysis, are used in the input. The framework developed in this work is not restricted to wall turbulence, and may be used in other flows to extract the properties of nonlinearities driving the observed coherent structures.

Author ORCIDs.
- U. Karban https://orcid.org/0000-0003-0803-0581;
- E. Martini https://orcid.org/0000-0002-3144-5702;
- A.V.G. Cavalieri https://orcid.org/0000-0003-4283-0232;
- L. Lesshafft https://orcid.org/0000-0002-2513-4553;
- P. Jordan https://orcid.org/0000-0001-8576-5587.

Appendix A. Linear operators used in resolvent analysis of channel flow

The linear operators used in (3.5) are given as

$$A = \begin{bmatrix} \mathcal{L}_k & -\nabla \\ \nabla^T & 0 \end{bmatrix}, \quad B = M = \begin{bmatrix} I & 0 & 0 \\ 0 & I & 0 \\ 0 & 0 & I \\ 0 & 0 & 0 \end{bmatrix} \quad \text{and} \quad C = \begin{bmatrix} I & 0 & 0 & 0 \\ 0 & I & 0 & 0 \\ 0 & 0 & I & 0 \end{bmatrix}, \quad (A1a\text{–}c)$$

where $\mathcal{L}_k$ is the spatial linear Navier–Stokes operator (McKeon 2017) given as

$$\mathcal{L}_k = \begin{bmatrix} -i\alpha U_x + \nabla^2/Re & -\partial_y U_x & 0 \\ 0 & -i\alpha U_x + \nabla^2/Re & 0 \\ 0 & 0 & -i\alpha U_x + \nabla^2/Re \end{bmatrix}, \quad (A2)$$

where $\nabla = [i\alpha,\ \partial_y,\ i\beta]^T$ and $\nabla^2 = \partial_y^2 - (\alpha^2 + \beta^2)$ are the gradient and Laplace operators, respectively.

REFERENCES

ABREU, L.I., CAVALIERI, A.V., SCHLATTER, P., VINUESA, R. & HENNINGSON, D.S. 2020*a* Resolvent modelling of near-wall coherent structures in turbulent channel flow. *Intl J. Heat Fluid Flow* **85**, 108662.

ABREU, L.I., CAVALIERI, A.V.G., SCHLATTER, P., VINUESA, R. & HENNINGSON, D.S. 2020*b* Spectral proper orthogonal decomposition and resolvent analysis of near-wall coherent structures in turbulent pipe flows. *J. Fluid Mech.* **900**, A11.

ADRIAN, R.J. 2007 Hairpin vortex organization in wall turbulence. *Phys. Fluids* **19**, 41301.

AGOSTINI, L. & LESCHZINER, M. 2017 Spectral analysis of near-wall turbulence in channel flow at $Re_\tau = 4200$ with emphasis on the attached-eddy hypothesis. *Phys. Rev. Fluids* **2**, 014603.

DEL ÁLAMO, J.C. & JIMÉNEZ, J. 2003 Spectra of the very large anisotropic scales in turbulent channels. *Phys. Fluids* **15**, L41.

AMARAL, F.R., CAVALIERI, A.V., MARTINI, E., JORDAN, P. & TOWNE, A. 2021 Resolvent-based estimation of turbulent channel flow using wall measurements. *J. Fluid Mech.* **927**, A17.

BAARS, W.J., HUTCHINS, N. & MARUSIC, I. 2017 Self-similarity of wall-attached turbulence in boundary layers. *J. Fluid Mech.* **823**, R2.

BALTZER, J., ADRIAN, R. & WU, X. 2010 Turbulent boundary layer structure identification via POD. In *Proceedings of the Summer Program 2010*, pp. 55–64. Center for Turbulence Research, Stanford University.

BORÉE, J. 2003 Extended proper orthogonal decomposition: a tool to analyse correlated events in turbulent flows. *Exp. Fluids* **35** (2), 188–192.

BRANDT, L. 2014 The lift-up effect: the linear mechanism behind transition and turbulence in shear flows. *Eur. J. Mech. B/Fluids* **47**, 80–96.

CAVALIERI, A.V.G., JORDAN, P. & LESSHAFFT, L. 2019 Wave-packet models for jet dynamics and sound radiation. *Appl. Mech. Rev.* **71** (2), 020802.

CHANDRAN, D., BAIDYA, R., MONTY, J.P. & MARUSIC, I. 2017 Two-dimensional energy spectra in high-Reynolds-number turbulent boundary layers. *J. Fluid Mech.* **826**, R1.

CHANDRAN, D., MONTY, J.P. & MARUSIC, I. 2020 Spectral-scaling-based extension to the attached eddy model of wall turbulence. *Phys. Rev. Fluids* **5**, 104606.

CHENG, C., LI, W., LOZANO-DURÁN, A. & LIU, H. 2020 Uncovering Townsend's wall-attached eddies in low-Reynolds-number wall turbulence. *J. Fluid Mech.* **889**, A29.

CHEVALIER, M., HŒPFFNER, J., BEWLEY, T.R. & HENNINGSON, D.S. 2006 State estimation in wall-bounded flow systems. Part 2. Turbulent flows. *J. Fluid Mech.* **552**, 167–187.

COSSU, C. & HWANG, Y. 2017 Self-sustaining processes at all scales in wall-bounded turbulent shear flows. *Phil. Trans. R. Soc.* A **375**, 20160088.

CROW, S.C. & CHAMPAGNE, F.H. 1971 Orderly structure in jet turbulence. *J. Fluid Mech.* **48**, 547–591.

DAVIDSON, P.A., KROGSTAD, P.-Å. & NICKELS, T.B. 2006a A refined interpretation of the logarithmic structure function law in wall layer turbulence. *Phys. Fluids* **18**, 065112.

DAVIDSON, P.A., NICKELS, T.B. & KROGSTAD, P.-Å. 2006b The logarithmic structure function law in wall-layer turbulence. *J. Fluid Mech.* **550**, 51–60.

EITEL-AMOR, G., ÖRLÜ, R., SCHLATTER, P. & FLORES, O. 2015 Hairpin vortices in turbulent boundary layers. *Phys. Fluids* **27**, 025108.

HELLSTRÖM, L.H., MARUSIC, I. & SMITS, A.J. 2016 Self-similarity of the large-scale motions in turbulent pipe flow. *J. Fluid Mech.* **792**, R1.

HELLSTRÖM, L.H. & SMITS, A.J. 2017 Structure identification in pipe flow using proper orthogonal decomposition. *Phil. Trans. R. Soc.* A **375**, 20160086.

HOARAU, C., BORÉE, J., LAUMONIER, J. & GERVAIS, Y. 2006 Analysis of the wall pressure trace downstream of a separated region using extended proper orthogonal decomposition. *Phys. Fluids* **18**, 055107.

HUSSAIN, A.K.F. 1986 Coherent structures and turbulence. *J. Fluid Mech.* **173**, 303–356.

HWANG, Y. 2015 Statistical structure of self-sustaining attached eddies in turbulent channel flow. *J. Fluid Mech.* **767**, 254–289.

HWANG, Y. & COSSU, C. 2010a Amplification of coherent streaks in the turbulent Couette flow: an input–output analysis at low Reynolds number. *J. Fluid Mech.* **643**, 333–348.

HWANG, Y. & COSSU, C. 2010b Self-sustained process at large scales in turbulent channel flow. *Phys. Rev. Lett.* **105**, 044505.

HWANG, Y. & ECKHARDT, B. 2020 Attached eddy model revisited using a minimal quasi-linear approximation. *J. Fluid Mech.* **894**, A23.

HWANG, J., LEE, J.H. & SUNG, H.J. 2020 Statistical behaviour of self-similar structures in canonical wall turbulence. *J. Fluid Mech.* **905**, A6.

HWANG, J., LEE, J., SUNG, H.J. & ZAKI, T.A. 2016 Inner–outer interactions of large-scale structures in turbulent channel flow. *J. Fluid Mech.* **790**, 128–157.

JIMÉNEZ, J. 2012 Cascades in wall-bounded turbulence. *Annu. Rev. Fluid Mech.* **44**, 27–45.

JODAI, Y. & ELSINGA, G.E. 2016 Experimental observation of hairpin auto-generation events in a turbulent boundary layer. *J. Fluid Mech.* **795**, 611–633.

JORDAN, P. & COLONIUS, T. 2013 Wave packets and turbulent jet noise. *Annu. Rev. Fluid Mech.* **45** (1), 173–195.

KARBAN, U., BUGEAT, B., MARTINI, E., TOWNE, A., CAVALIERI, A.V.G., LESSHAFFT, L., AGARWAL, A., JORDAN, P. & COLONIUS, T. 2020 Ambiguity in mean-flow-based linear analysis. *J. Fluid Mech.* **900**, R5.

KERHERVE, F., JORDAN, P., CAVALIERI, A., DELVILLE, J., BOGEY, C. & JUVÉ, D. 2012 Educing the source mechanism associated with downstream radiation in subsonic jets. *J. Fluid Mech.* **710**, 606–640.

LEE, C. & JIANG, X. 2019 Flow structures in transitional and turbulent boundary layers. *Phys. Fluids* **31**, 111301.

LESSHAFFT, L., SEMERARO, O., JAUNET, V., CAVALIERI, A.V.G. & JORDAN, P. 2019 Resolvent-based modeling of coherent wave packets in a turbulent jet. *Phys. Rev. Fluids* **4**, 063901.

LUMLEY, J.L. 1967 The structure of inhomogeneous turbulent flows. In *Proceedings of the International Colloquium on the Fine Scale Structure of the Atmosphere and Its Influence on Radio Wave Propagation* (ed. A.M. Yaglam & V.I. Tatarsky). Doklady Akademii Nauk SSSR.

LUMLEY, J.L. 1970 Toward a turbulent constitutive relation. *J. Fluid Mech.* **41** (2), 413–434.

MARTINI, E., CAVALIERI, A.V., JORDAN, P. & LESSHAFFT, L. 2019 Accurate frequency domain identification of ODEs with arbitrary signals. arXiv:1907.04787v3.

MARTINI, E., CAVALIERI, A.V.G., JORDAN, P., TOWNE, A. & LESSHAFFT, L. 2020 Resolvent-based optimal estimation of transitional and turbulent flows. *J. Fluid Mech.* **900**, A2.

MARUSIC, I. & MONTY, J.P. 2019 Attached eddy model of wall turbulence. *Annu. Rev. Fluid Mech.* **51**, 49–74.

MCKEON, B.J. 2017 The engine behind (wall) turbulence: perspectives on scale interactions. *J. Fluid Mech.* **817**, P1.

MCKEON, B.J. & SHARMA, A.S. 2010 A critical-layer framework for turbulent pipe flow. *J. Fluid Mech.* **658**, 336–382.

MOARREF, R., SHARMA, A.S., TROPP, J.A. & MCKEON, B.J. 2013 Model-based scaling of the streamwise energy density in high-Reynolds-number turbulent channels. *J. Fluid Mech.* **734**, 275–316.

MOLLO-CHRISTENSEN, E. 1967 Jet noise and shear flow instability seen from an experimenter's viewpoint. *Trans. ASME J. Appl. Mech.* **34**, 1–7.

MONTY, J.P., STEWART, J.A., WILLIAMS, R.C. & CHONG, M.S. 2007 Large-scale features in turbulent pipe and channel flows. *J. Fluid Mech.* **589**, 147–156.

MORRA, P., NOGUEIRA, P.A.S., CAVALIERI, A.V.G. & HENNINGSON, D.S. 2021 The colour of forcing statistics in resolvent analyses of turbulent channel flows. *J. Fluid Mech.* **907**, A24.

MORRA, P., SEMERARO, O., HENNINGSON, D.S. & COSSU, C. 2019 On the relevance of Reynolds stresses in resolvent analyses of turbulent wall-bounded flows. *J. Fluid Mech.* **867**, 969–984.

NOGUEIRA, P.A.S., MORRA, P., MARTINI, E., CAVALIERI, A.V.G. & HENNINGSON, D.S. 2021 Forcing statistics in resolvent analysis: application in minimal turbulent Couette flow. *J. Fluid Mech.* **908**, A32.

PERRY, A.E. & CHONG, M.S. 1982 On the mechanism of wall turbulence. *J. Fluid Mech.* **119**, 173–217.

PERRY, A.E., HENBEST, S. & CHONG, M.S. 1986 A theoretical and experimental study of wall turbulence. *J. Fluid Mech.* **165**, 163–199.

PICARD, C. & DELVILLE, J. 2000 Pressure velocity coupling in a subsonic round jet. *Intl J. Heat Fluid Flow* **21** (3), 359–364.

PICKERING, E.M., RIGAS, G., SIPP, D., SCHMIDT, O.T. & COLONIUS, T. 2019 Eddy viscosity for resolvent-based jet noise models. In *25th AIAA/CEAS Aeroacoustics Conference.* AIAA Paper 2019-2454.

ROBINSON, S. 1991 Coherent motions in the turbulent boundary layer. *Annu. Rev. Fluid Mech.* **23**, 601–639.

ROSENBERG, K., SYMON, S. & MCKEON, B.J. 2019 Role of parasitic modes in nonlinear closure via the resolvent feedback loop. *Phys. Rev. Fluids* **4**, 052601.

SCHLEGEL, M., NOACK, B.R., JORDAN, P., DILLMANN, A., GRÖSCHEL, E., SCHRÖDER, W., WEI, M., FREUND, J.B., LEHMANN, O. & TADMOR, G. 2012 On least-order flow representations for aerodynamics and aeroacoustics. *J. Fluid Mech.* **697**, 367–398.

SCHMID, P.J. 2010 Dynamic mode decomposition of numerical and experimental data. *J. Fluid Mech.* **656**, 5–28.

SCHMIDT, O.T., TOWNE, A., RIGAS, G., COLONIUS, T. & BRÈS, G.A. 2018 Spectral analysis of jet turbulence. *J. Fluid Mech.* **855**, 953–982.

SEN, M., BHAGANAGAR, K. & JUTTIJUDATA, V. 2007 Application of proper orthogonal decomposition (POD) to investigate a turbulent boundary layer in a channel with rough walls. *J. Turbul.* **8**, N41.

SHARMA, A.S., MOARREF, R. & MCKEON, B.J. 2017 Scaling and interaction of self-similar modes in models of high Reynolds number wall turbulence. *Phil. Trans. R. Soc.* A **375** (2089), 20160089.

SKOULOUDIS, N. & HWANG, Y. 2021 Scaling of turbulence intensities up to $Re_\tau = 10^6$ with a resolvent-based quasilinear approximation. *Phys. Rev. Fluids* **6**, 034602.

SYMON, S., ILLINGWORTH, S.J. & MARUSIC, I. 2021 Energy transfer in turbulent channel flows and implications for resolvent modelling. *J. Fluid Mech.* **911**, A3.

TAIRA, K., BRUNTON, S.L., DAWSON, S.T., ROWLEY, C.W., COLONIUS, T., MCKEON, B.J., SCHMIDT, O.T., GORDEYEV, S., THEOFILIS, V. & UKEILEY, L.S. 2017 Modal analysis of fluid flows: an overview. *AIAA J.* **55**, 4013–4041.

TOMKINS, C.D. & ADRIAN, R.J. 2003 Spanwise structure and scale growth in turbulent boundary layers. *J. Fluid Mech.* **490**, 37–74.

TOWNE, A., COLONIUS, T., JORDAN, P., CAVALIERI, A.V. & BRÈS, G.A. 2015 Stochastic and nonlinear forcing of wavepackets in a Mach 0.9 jet. In *21st AIAA/CEAS Aeroacoustics Conference.* AIAA Paper 2015-2217.

TOWNE, A., LOZANO-DURÁN, A. & YANG, X. 2020 Resolvent-based estimation of space–time flow statistics. *J. Fluid Mech.* **883**, A17.

TOWNE, A., SCHMIDT, O.T. & COLONIUS, T. 2018 Spectral proper orthogonal decomposition and its relationship to dynamic mode decomposition and resolvent analysis. *J. Fluid Mech.* **847**, 821–867.

TOWNSEND, A.A. 1951 The structure of the turbulent boundary layer. *Math. Proc. Camb. Phil. Soc.* **47**, 375–395.

TOWNSEND, A.A. 1976 *The Structure of Turbulent Shear Flow*, 2nd edn. Cambridge University Press.

WEI, T., FIFE, P., KLEWICKI, J. & MCMURTRY, P. 2005 Properties of the mean momentum balance in turbulent boundary layer, pipe and channel flows. *J. Fluid Mech.* **522**, 303–327.

WU, X. & MOIN, P. 2009 Direct numerical simulation of turbulence in a nominally zero-pressure-gradient flat-plate boundary layer. *J. Fluid Mech.* **630**, 5–41.

YANG, X.I.A. & LOZANO-DURÁN, A. 2017 A multifractal model for the momentum transfer process in wall-bounded flows. *J. Fluid Mech.* **824**, R2.

ZARE, A., JOVANOVIĆ, M.R. & GEORGIOU, T.T. 2017 Colour of turbulence. *J. Fluid Mech.* **812**, 636–680.